

The Leading, Interdecadal Eigenmode of the Atlantic Meridional Overturning Circulation in a Realistic Ocean Model

FLORIAN SÉVELLEC

Ocean and Earth Science, National Oceanographic Centre Southampton, University of Southampton, Southampton, United Kingdom

ALEXEY V. FEDOROV

Department of Geology and Geophysics, Yale University, New Haven, Connecticut

(Manuscript received 6 January 2011, in final form 27 June 2012)

ABSTRACT

Variations in the strength of the Atlantic meridional overturning circulation (AMOC) are a major potential source of decadal and longer climate variability in the Atlantic. This study analyzes continuous integrations of tangent linear and adjoint versions of an ocean general circulation model [Océan Parallélisé (OPA)] and rigorously shows the existence of a weakly damped oscillatory eigenmode of the AMOC centered in the North Atlantic Ocean and controlled solely by linearized ocean dynamics. In this particular GCM, the mode period is roughly 24 years, its e -folding decay time scale is 40 years, and it is the least-damped oscillatory mode in the system. Its mechanism is related to the westward propagation of large-scale temperature anomalies in the northern Atlantic in the latitudinal band between 30° and 60°N. The westward propagation results from a competition among mean eastward zonal advection, equivalent anomalous westward advection caused by the mean meridional temperature gradient, and westward propagation typical of long baroclinic Rossby waves. The zonal structure of temperature anomalies alternates between a dipole (corresponding to an anomalous AMOC) and anomalies of one sign (yielding no changes in the AMOC). Further, it is shown that the system is nonnormal, which implies that the structure of the least-damped eigenmode of the tangent linear model is different from that of the adjoint model. The “adjoint” mode describes the sensitivity of the system (i.e., it gives the most efficient patterns for exciting the leading eigenmode). An idealized model is formulated to highlight the role of the background meridional temperature gradient in the North Atlantic for the mode mechanism and the system nonnormality.

1. Introduction

Variability of the Atlantic meridional overturning circulation (AMOC) is believed to be a major source of climate variability in the Atlantic on time scales from decadal to centennial and longer. Observational, modeling, and theoretical studies suggest a number of potential mechanisms and climate modes that can lead to temporal variations in the AMOC [for a recent review, see Yoshimori et al. (2010)]. Similarly, comprehensive climate models show a broad diversity of the simulated AMOC variability—its amplitude, typical periods, and the dominant mode vary greatly from one model to the next (e.g., Solomon et al. 2007). The mechanisms of this

variability remain a subject of continuing debates. The present work focuses on a robust interdecadal oscillatory mode (an eigenmode) controlled by ocean dynamics in the North Atlantic Ocean.

Many studies of climate variability in the Atlantic concentrate on the dynamics of the Atlantic multidecadal oscillation (AMO)—climate variability with periods between 50 and 70 years (Kushnir 1994; Delworth and Mann 2000) typically associated with variations in the AMOC intensity of the order of several Sverdrups (1 Sv $\equiv 10^6 \text{ m}^3 \text{ s}^{-1}$; Knight et al. 2005). The AMO can exert strong impacts on climate, affecting hurricane activity over the North Atlantic (Goldenberg et al. 2001) and precipitation over North America (Sutton and Hodson 2005). Sutton and Hodson (2003) linked the climate change over the North Atlantic during the period 1871–1999 to the AMO.

An AMO-like multidecadal variability has been studied in climate models of different complexity (Yoshimori

Corresponding author address: Florian Sévellec, Ocean and Earth Science, University of Southampton, Waterfront campus, European Way, Southampton SO14 3ZH, United Kingdom.
E-mail: florian.sevellec@noc.soton.ac.uk

et al. 2010; Latif 1997). Several physical mechanisms for the AMO have been proposed, including changes in the subtropical gyre (Dong and Sutton 2005; D'Orgeville and Peltier 2009; Cheng et al. 2004) or changes in the subpolar gyre that alter the heat budget of the Labrador Sea (Danabasoglu 2008), just to give a few examples.

Recent observational studies show the existence not only of the 50–70-yr variability, but also of variability in the 20–30-yr band (Frankcombe et al. 2008). This shorter-period, interdecadal variability can be identified by looking at temperature or sea level height (SLH) variations in latitudinal bands (instead of using the average sea surface temperature over the North Atlantic, which is a classical AMO index). This interdecadal variability is characterized by the westward propagation of temperature anomalies. Analyzing zonal variations in SLH, Frankcombe and Dijkstra (2009) found such variability both in observations and climate models. The authors hypothesize that the AMO might have a strong signature at 20–30 yr in addition to the 50–70-yr band more commonly associated with the AMO. They point out, however, that the relatively short records analyzed in their study may have overemphasized shorter periods in the data.

Studies with idealized ocean models also confirm the existence of such an interdecadal mode characterized by westward propagation. Several theories have been put forward to explain this mode: for example, Huck et al. (1999) and Colin de Verdière and Huck (1999) suggest that this mode is associated with large-scale Rossby waves propagating westward across the north–south thermal gradient. In contrast, te Raa and Dijkstra (2002) interpret the mode propagation as a result of interaction between ocean stratification and an anomalous vertical flow induced by a nondivergent geostrophic flow along the basin boundary. However, more recently te Raa et al. (2004) and Dijkstra et al. (2006) have shown that the mode does not change when an idealized rectangular basin is replaced with the realistic North Atlantic coastline.

Two recent studies suggest that this interdecadal mode can be sustained by atmospheric noise (Frankcombe et al. 2009; Sévellec et al. 2009), but they disagree on some of the properties of the mode, such as whether the system is normal or nonnormal (i.e., the eigenmodes form an orthogonal or a nonorthogonal basis) (e.g., Ioannou 1995). Frankcombe et al. (2009) has argued that the decadal time scale is a signature of a normal mode; however, Sévellec et al. (2009) demonstrated the importance of the nonnormality for setting the amplitude of decadal variability [as discussed by Farrell and Ioannou (1996), climate variability excited by stochastic forcing in a nonnormal system should be stronger than in an analogous normal system]. In addition, the role of freshwater fluxes for the

interdecadal mode has been also discussed, in idealized settings, by Chen and Ghil (1995) and, more recently, by te Raa and Dijkstra (2003) and Sévellec et al. (2009).

A fundamental question that has not been rigorously addressed yet is whether an interdecadal natural mode of oscillation controlled by ocean dynamics (an eigenmode rather than a mode of variability) would exist in realistic ocean conditions. This is the central question of the present study. Specifically, using a tangent linear version of a realistic ocean GCM, we extract a weakly damped eigenmode of the system. In our calculations, the mode period is close to 24 years and the damping time scale is about 40 years. We refer to this mode as weakly damped since the decay time scale is roughly 70% longer than the period, which is sufficiently long to distinguish clearly many cycles of the oscillation throughout the time integration of the model (Fig. 2, discussed in greater detail below).

In this study, we explore the underlying mechanisms and key properties of this eigenmode. We show that the westward propagation of temperature anomalies is indeed critical for this mode and results from the competition among (i) the mean eastward zonal advection, (ii) the equivalent anomalous westward advection that depends on the mean meridional thermal gradient in the ocean, and (iii) the westward advection typical of long baroclinic Rossby waves (related to the β -effect).

Using the tangent linear and adjoint versions of this GCM and an idealized model, we also examine the role of nonnormality in ocean dynamics. We demonstrate that the structures of the least-damped oscillatory mode of the forward model and that in the adjoint (i.e., the biorthogonal mode) are drastically different. We also show that salinity anomalies and changes in the deep ocean play only a minor part in the oscillatory mechanism of the interdecadal mode; however, both effects are important for exciting this mode via a transient non-normal growth in the system.

The structure of the paper is as follows: In section 2, we describe the ocean GCM and the methodology we use to obtain the least-damped eigenmodes of the tangent linear model and its adjoint. In section 3, we discuss the properties of the eigenmode and the adjoint mode. In section 4, we formulate an idealized model to further examine the properties of the oscillation. In section 5, we summarize the implications of this study.

2. Methods

a. Ocean models and model configurations

The ocean GCM we use in this study is Océan Parallélisé (OPA) 8.2 (Madec et al. 1998) in its 2° global configuration

(ORCA2; Madec and Imbard 1996). There are 31 levels in the vertical; the level thickness varies from 10 m at the surface to 500 m at depth. The model is integrated using an Arakawa C grid and the z coordinates, and the rigid-lid approximation.

The present model configuration makes use of the following parameterizations: convection is parameterized by an increase in the vertical diffusion when the ocean vertical stratification is unstable; double diffusion is taken into account by two different terms for mixing temperature and salinity; eddy-induced velocities are described by the Gent and McWilliams (1990) approximation; the viscosity coefficients follow the turbulent closure scheme of Blanke and Delecluse (1993) and are functions of longitude, latitude, and depth; and tracer diffusivities vary in longitude and latitude (Redi 1982).

The tangent linear and adjoint models are provided by the OPATAM (which stands for OPA tangent adjoint model) code (Weaver et al. 2003), which is based on the linearization of OPA's primitive equations of motions with respect to the ocean seasonally varying basic state of the ocean.

For the present study, we impose surface heat and freshwater fluxes (from the model climatology) and do not use surface restoring. These fluxes are computed by running the full nonlinear model in a forced mode. This approach produces a realistic seasonal cycle for the linear and adjoint models, but reduces the damping and allows SST anomalies to develop more easily (Huck and Vallis 2001; Arzel et al. 2006; Sévellec et al. 2009). For details see below.

Several additional approximations have been introduced for the tangent linear and adjoint models. The viscosity coefficients, the tracer diffusivities, and the eddy-induced advection are calculated only for the basic ocean state; further variations in those parameters are neglected.

b. Ocean basic state and linearization

1) THE OCEAN BASIC STATE

The seasonally varying basic state of the ocean, here also referred to as the annual model "trajectory," is obtained by direct integration of the OPA subject to the climatological surface boundary forcing (varying with the annual cycle). For the forcing, we use European Centre for Medium-Range Weather Forecasts (ECMWF) heat fluxes averaged for the interval 1979–93, the European Remote Sensing satellite (ERS) wind stress blended with the Tropical Atmosphere Ocean (TAO) data between 1993 and 1996, and an estimate of the climatological river runoff. In addition, we apply a surface temperature restoring to the Reynolds climatological SSTs averaged

from 1982 to 1989, together with a surface salinity restoring to the Levitus (1989) climatology. A restoring term to the Levitus climatological values of temperature and salinity is applied in the Red and Mediterranean Seas (we emphasize that no restoring is used in the linear models). Starting with the Levitus climatology as the initial conditions, the model produces a quasi-stationary annual cycle of the ocean basic state after 200 years of integration.

The Atlantic meridional overturning circulation in the full GCM (Fig. 1) is characterized by the northward mass transport above the thermocline, a southward return flow between 1500 and 3000 m, and a second cell below 3000 m associated with the Antarctic Bottom Water. The maximum volume transport of the AMOC is around 14 Sv, which is slightly below but still within the error bars of the observations (18 ± 5 Sv; Talley et al. 2003). The AMOC poleward heat transport reaches 0.8 PW at 25°N, whereas estimations from inverse calculations and hydrographic sections give 1.3 PW at 24°N (Ganachaud and Wunsch 2000).

As expected, the SST field develops a strong meridional gradient in the northern Atlantic, especially across the North Atlantic Current (NAC), and a salinity maximum at about 20°N (Fig. 1). The barotropic streamfunction shows an intense subtropical gyre and a weaker subpolar gyre centered at about 60°N. The two gyres are separated by the NAC.

Overall, the full nonlinear model produces a realistic (seasonally varying) basic state of the ocean. Next, we will conduct a linear stability analysis of this ocean state.

2) EIGENMODE COMPUTATIONS

The goal of these experiments is to identify the least-damped eigenmodes of the tangent linear and adjoint models (linearized with respect to the seasonally varying basic state) by conducting long continuous integrations and applying a Poincaré section to eliminate the seasonal cycle from consideration (Strogatz 1994). Alternatively, we could use the Floquet theorem and transform the periodic system to a traditional linear system with constant coefficients. However, in our case, obtaining the eigenmodes requires the diagonalization of a matrix of the size $3\,400\,011 \times 3\,400\,011$. This task goes beyond the limits of our computational capabilities; consequently, we apply the long integration approach. As demonstrated below, such an approach should reveal the least-damped eigenmode in the system.

A nonautonomous dynamical system, such as that of a GCM, can be written as

$$d_t|\mathbf{U}\rangle = \mathcal{N}(|\mathbf{U}\rangle, t), \quad (1)$$

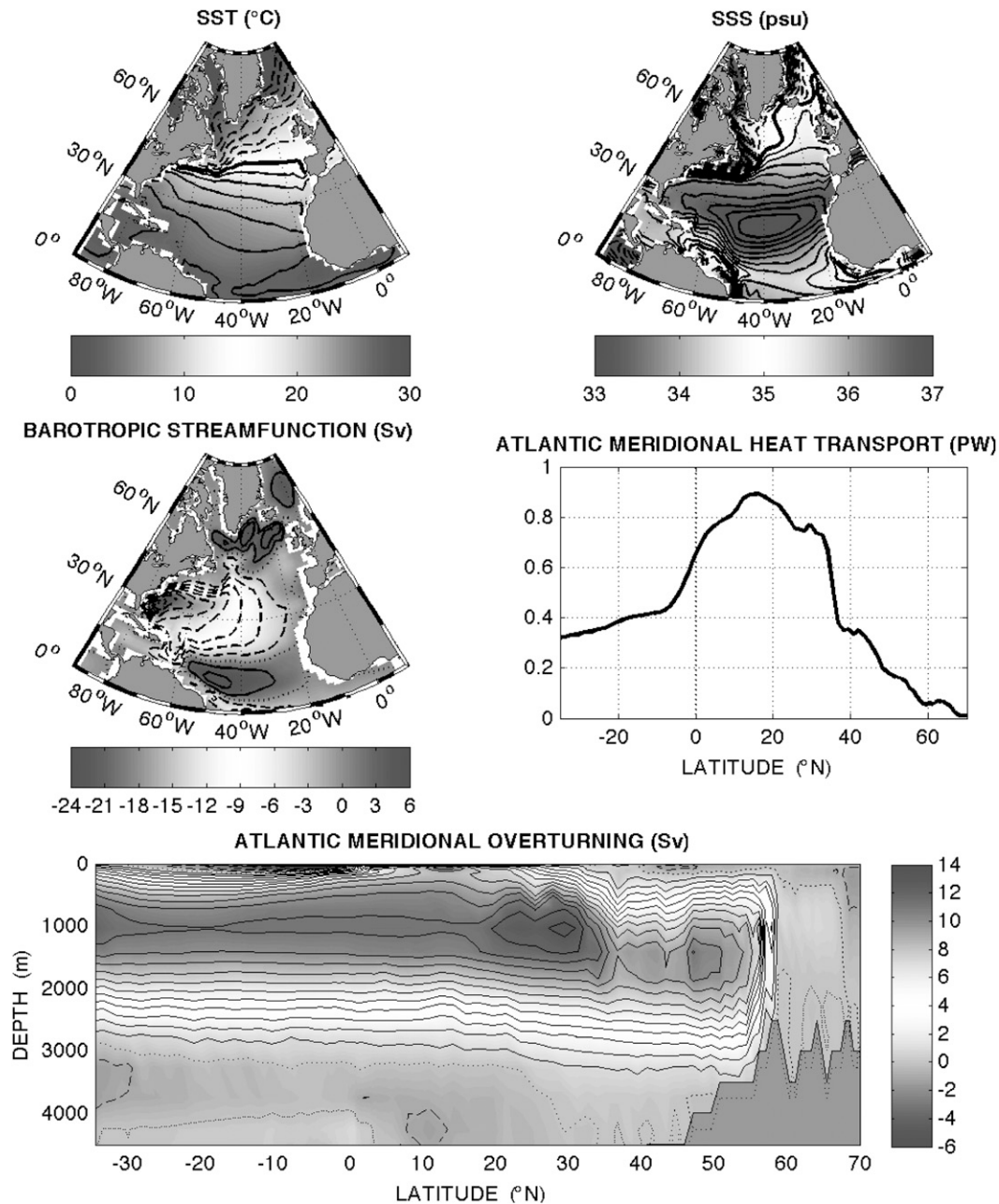


FIG. 1. The mean state of the ocean as reproduced by the full GCM. (Top left) Sea surface temperature; contour interval (CI) is 2°C, the thick solid line corresponds to 15°C, solid and dashed lines correspond to higher and lower values, respectively. (Top right) Sea surface salinity; CI is 0.25 psu, the thick solid line corresponds to 35 psu, and solid and dashed lines correspond to higher and lower values, respectively. (Middle left) Barotropic streamfunction; CI is 3 Sv. (Middle right) The Atlantic Ocean meridional heat transport as a function of latitude. (Bottom) Zonally averaged streamfunction for the Atlantic meridional overturning circulation; CI is 1 Sv. In the two streamfunction plots, solid, dashed, and dotted lines indicate positive, negative, and zero values, respectively. Seasonal variations are not shown.

where t is time, $|\mathbf{U}\rangle$ the state vector of all prognostic variables, and \mathcal{N} a time-dependent nonlinear operator. We also define the notation $\langle \mathbf{U} |$ through the Euclidian norm defined by the scalar product (or dot product) $\langle \mathbf{U} | \mathbf{U} \rangle$, where temperature and salinity are weighted in

terms of density and the relative volume of each grid box (the model grid is not uniform). After we decompose the state vector as $|\mathbf{U}\rangle = |\bar{\mathbf{U}}\rangle + |\mathbf{u}\rangle$, where $|\bar{\mathbf{U}}\rangle$ is the nonlinear annual trajectory and $|\mathbf{u}\rangle$ is a perturbation, the time evolution of the perturbation is described by a linear equation:

$$d_t|\mathbf{u}\rangle = \left. \frac{\partial \mathcal{N}}{\partial |\mathbf{u}\rangle} \right|_{|\bar{\mathbf{u}}\rangle}. \quad (2)$$

We rewrite this latter equation using a nonautonomous propagator \mathbf{M} that connects perturbations at time t_1 to those at time t_2 as

$$|\mathbf{u}(t_2)\rangle = \mathbf{M}(t_2, t_1)|\mathbf{u}(t_1)\rangle. \quad (3)$$

In our computations, \mathbf{M} is a matrix.

Further, we can simplify (3) by eliminating the seasonal cycle from consideration and using the first recurrence map analysis (also called a Poincaré section). This procedure removes one codimension, allowing us to study stability of a fixed point instead of a limit cycle (Strogatz 1994). Specifically, we extract from the matrix \mathbf{M} all points that occur at the same time of the seasonal cycle every year ($\Delta t = 1$ yr)—for example, the points that occur on 31 December t^* . Because the only time dependency in the linearized operator comes from the climatological seasonal cycle, this procedure yields a new autonomous dynamical system (denoted by $\tilde{\cdot}$):

$$\tilde{\mathbf{M}}(t = n\Delta t) = \mathbf{M}(t^* + n\Delta t, t^*), \quad (4)$$

where n is an integer representing the number of seasonal cycles and t is the new time.

The linear and adjoint models of this system can be rewritten in term of their eigenvectors as

$$\tilde{\mathbf{M}}(t) = \sum_j |\mathbf{u}_j\rangle e^{\lambda_j t} \langle \mathbf{u}_j^\dagger| \quad \text{and} \quad (5a)$$

$$\tilde{\mathbf{M}}^\dagger(t) = \sum_j |\mathbf{u}_j^\dagger\rangle e^{\lambda_j^* t} \langle \mathbf{u}_j|, \quad (5b)$$

where $\tilde{\mathbf{M}}^\dagger$ is the adjoint propagator matrix (defined through the Euclidian norm), $|\mathbf{u}_j\rangle$ and λ_j are the eigenvectors and eigenvalues of $\tilde{\mathbf{M}}$, $|\mathbf{u}_j^\dagger\rangle$ and λ_j^* are the eigenvectors and eigenvalues of $\tilde{\mathbf{M}}^\dagger$ (where $*$ denotes a complex conjugate), and the sum over j represents summation over all eigenvectors (corresponding to the number of degrees of freedom in the discretized model).

Because e -folding decay scales of the eigenmodes differ from each other [$1/\Re(\lambda_j)$, where \Re denotes the real part], on long time scales ($t \rightarrow \infty$) only the least-damped eigenmode will persist: that is, the eigenmode with the minimum value of $\Re(\lambda_j)$. We will denote this mode by index $j = 1$. Then, the tangent linear and adjoint models yield

$$\lim_{t \rightarrow \infty} \tilde{\mathbf{M}}(t) = \lim_{t \rightarrow \infty} |\mathbf{u}_1\rangle e^{\lambda_1 t} \langle \mathbf{u}_1^\dagger| \quad \text{and} \quad (6a)$$

$$\lim_{t \rightarrow \infty} \tilde{\mathbf{M}}^\dagger(t) = \lim_{t \rightarrow \infty} |\mathbf{u}_1^\dagger\rangle e^{\lambda_1^* t} \langle \mathbf{u}_1|. \quad (6b)$$

Thus, if $|\mathbf{u}(0)\rangle$ is an arbitrary initial condition, on long time scales the outputs $|\mathbf{u}(t)\rangle$ of the tangent linear and adjoint models are controlled by their least-damped eigenmodes:

$$\begin{aligned} |\mathbf{u}(\infty)\rangle &= \lim_{t \rightarrow \infty} \tilde{\mathbf{M}}(t)|\mathbf{u}(0)\rangle \\ &= \lim_{t \rightarrow \infty} |\mathbf{u}_1\rangle e^{\lambda_1 t} \langle \mathbf{u}_1^\dagger|\mathbf{u}(0)\rangle \propto |\mathbf{u}_1\rangle \quad \text{and} \end{aligned} \quad (7a)$$

$$|\mathbf{u}(\infty)\rangle = \lim_{t \rightarrow \infty} \tilde{\mathbf{M}}^\dagger(t)|\mathbf{u}(0)\rangle = \lim_{t \rightarrow \infty} |\mathbf{u}_1^\dagger\rangle e^{\lambda_1^* t} \langle \mathbf{u}_1|\mathbf{u}(0)\rangle \propto |\mathbf{u}_1^\dagger\rangle. \quad (7b)$$

Accordingly, to obtain the least-damped eigenmodes for these two cases, we have conducted several long time integrations of the tangent linear model and its adjoint, each lasting 500 yr. For the forward model, we used four different initial conditions $|\mathbf{u}(0)\rangle$ to check the convergence of the asymptotic output $|\mathbf{u}(\infty)\rangle$ to the same eigenvector $|\mathbf{u}_1\rangle$. For the adjoint model, we used three different initial conditions to check the convergence to $|\mathbf{u}_1^\dagger\rangle$. Note that in the latter case, the integration was conducted from the initial conditions but backward in time.

The flux surface boundary conditions used in this study (for both temperature and salinity) also allow two null modes. These modes correspond to adding constants to temperature or salinity anomalies, which would not change the shape of those fields or affect the dynamics. To avoid the null mode in the computation of the eigenmode, one could use initial perturbations with zero mean temperature and salinity, or remove the means after the time integration.

Note that during the review of this paper, we have extended the original calculations to more than 3000 yr. The only oscillatory mode we could find was the same interdecadal eigenmode as described in the paper. However, we did find a purely damped eigenmode with a longer damping time scale (on the order of 1000 yr) associated with the slow vertical adjustment of the ocean thermocline. We hypothesize that this mode controls climate drift in ocean GCMs and possibly the deep ocean response to climate change. Nevertheless, since this mode does not induce AMOC variability, it is not considered in this study.

3. Results

a. The model least-damped oscillatory eigenmode

Analyzing the output of the tangent linear model reveals the existence in the system of a damped oscillatory eigenmode centered in the North Atlantic with a period of about 24 yr and an e -folding decay time scale of 40 yr

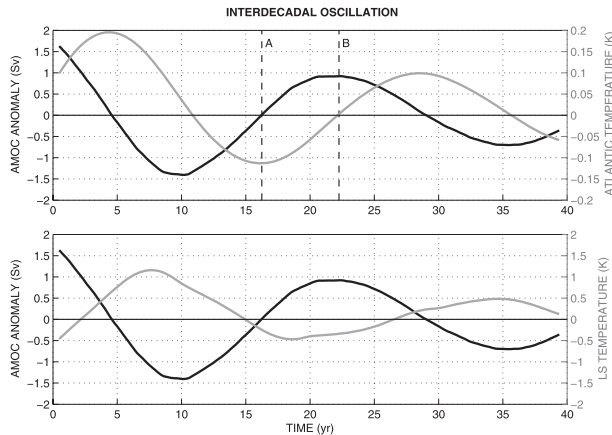


FIG. 2. Temporal evolution of the least-damped eigenmode of the tangent linear model. (top) Variations of the AMOC volume transport (black line) and average temperature in the northern Atlantic (gray line). The AMOC streamfunction is evaluated between 0 and 1200 m over 34°–62°N; temperature is averaged over the total depth of the ocean between 34° and 62°N and 85°W and 12°E. (bottom) Variations of the AMOC volume transport (black line) and the Labrador Sea temperature (gray line, LS). The vertical dashed lines labeled A and B denote two phases of the oscillation separated by a quarter-period. The spatial structure of the mode for the two phases is shown in Figs. 3 and 7.

(Fig. 2). As discussed in the previous section, this is the least-damped oscillatory eigenmode identified in the model. This interdecadal mode exhibits a nearly quadrature phase relationship between variations in the AMOC strength and the temperature averaged over the northern Atlantic (Fig. 2, top). The heat content of the Labrador Sea appears to be a good precursor, by roughly 2 yr, of the AMOC changes (Fig. 2, bottom). Similar phase relationships among changes in the ocean heat content, the Labrador Sea heat content, and the AMOC transport on multidecadal time scales have been discussed by Danabasoglu (2008).

Temperature variations associated with the interdecadal mode in our model are especially pronounced in the upper 1000 m of the northern Atlantic Ocean between 30° and 60°N (Fig. 3, top). The temporal evolution of the mode exhibits two distinct (quadrature) phases: phases A and B (Fig. 2, top). Phase A is characterized by a strong anomaly of the zonally averaged temperature in the upper ocean but almost no anomaly in the ocean large-scale meridional overturning, whereas phase B has very weak anomaly in zonally averaged temperature but a strong anomaly in the overturning streamfunction (Fig. 3).

During the first phase of the oscillation (A), a cooling in the upper ocean induces anomalous horizontal velocity around the temperature or, more accurately, density anomaly (Fig. 3, top left). The anomalous geostrophic flow (cyclonic for a cold anomaly) is able to modify both

the subtropical and subpolar gyres. In the upper ocean, this flow acts on the background meridional temperature gradient, bringing warm waters from the south into the eastern part of the basin and cold waters from the north into the western part. This mechanism, together with the β -effect, effectively leads to the westward propagation of the initial temperature anomaly. At depth, in the absence of a mean temperature gradient comparable to that in the upper ocean, the anomalous velocity has little effect on temperature. Also, since the anomalous circulation occurs around a one-sign temperature anomaly (versus a dipole), the southward and northward velocities largely compensate each other and contribute little to the meridional overturning (Fig. 3, bottom left).

The resulting westward propagation of the cold temperature anomaly and the anomalous flow from the south causes the development of a warm temperature anomaly on the right flank of the initial anomaly (Fig. 4). This newly formed dipole pattern of temperature (cold–warm) becomes most pronounced by the second phase of the oscillation (phase B in Fig. 3, right panels). In turn, the zonal density gradient within the temperature dipole generates a northward geostrophic velocity anomaly in the upper ocean (via thermal wind balance) and a positive anomaly in the meridional overturning. The westward propagation of alternating temperature anomalies is clearly evident from a Hovmöller diagram for the mode with the amplitude decay suppressed (Fig. 5).

In the discussion above, we have implicitly assumed that the background meridional density gradient is controlled by temperature ($|\alpha\partial_y\bar{T}| \gg |\beta\partial_y\bar{S}|$), where α and β are the thermal expansion and haline contraction coefficients, respectively. This assumption holds fairly well in the Atlantic north of 30°N (Fig. 6). Therefore, anomalous meridional velocity in this region acts mostly on the mean temperature rather than salinity gradient when generating density anomalies. That is why the mode dynamics are predominantly controlled by temperature variations.

Nevertheless, the oscillatory mode does have a salinity component (Fig. 7). Even though temperature and salinity anomalies have similar shapes and propagation characteristics, salinity anomalies act to reduce the effect of temperature anomalies on density (cf. Figs. 3 and 7). This behavior is a consequence of the opposite effects on density of the mean meridional gradients of temperature and salinity. For example, anomalous northward advection extracts from the mean fields positive anomalies in temperature and salinity. However, the two have opposite effects on density, so that the latter partially compensates the effect of the former. In simplified models such compensation has been discussed by Huck et al. (1999), Huck and Vallis (2001), te Raa and Dijkstra (2002), and Sévellec et al. (2009).

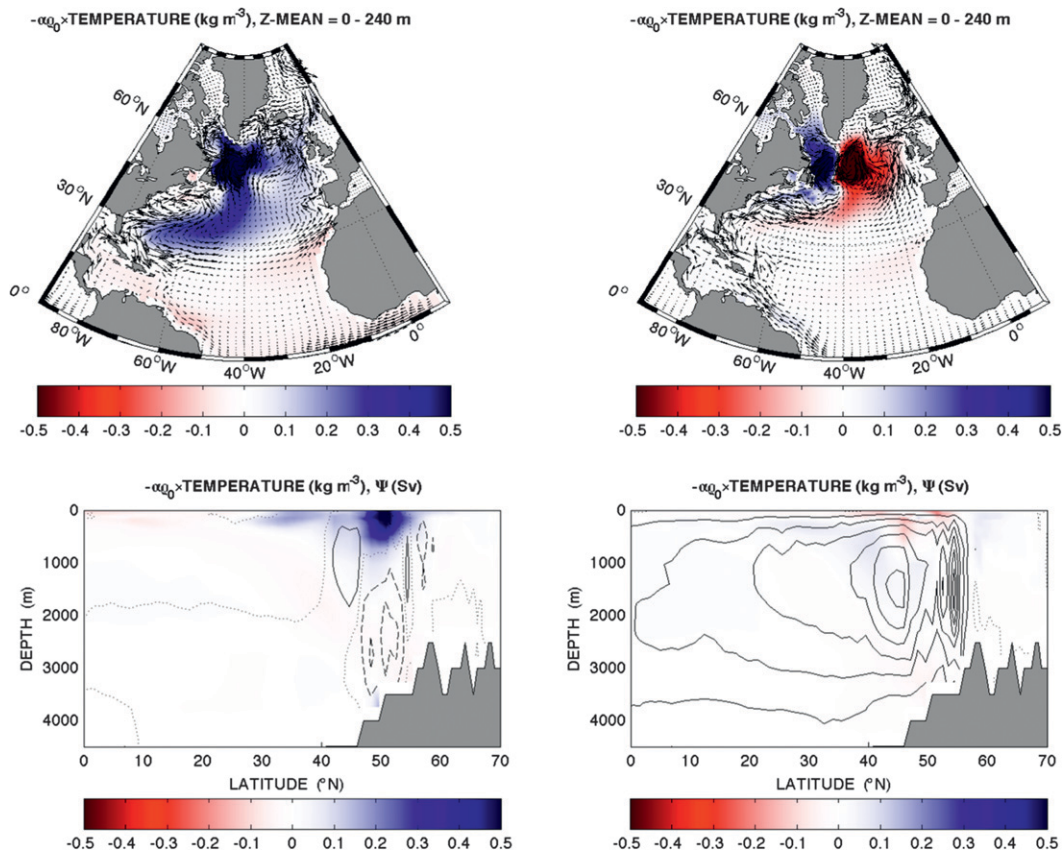


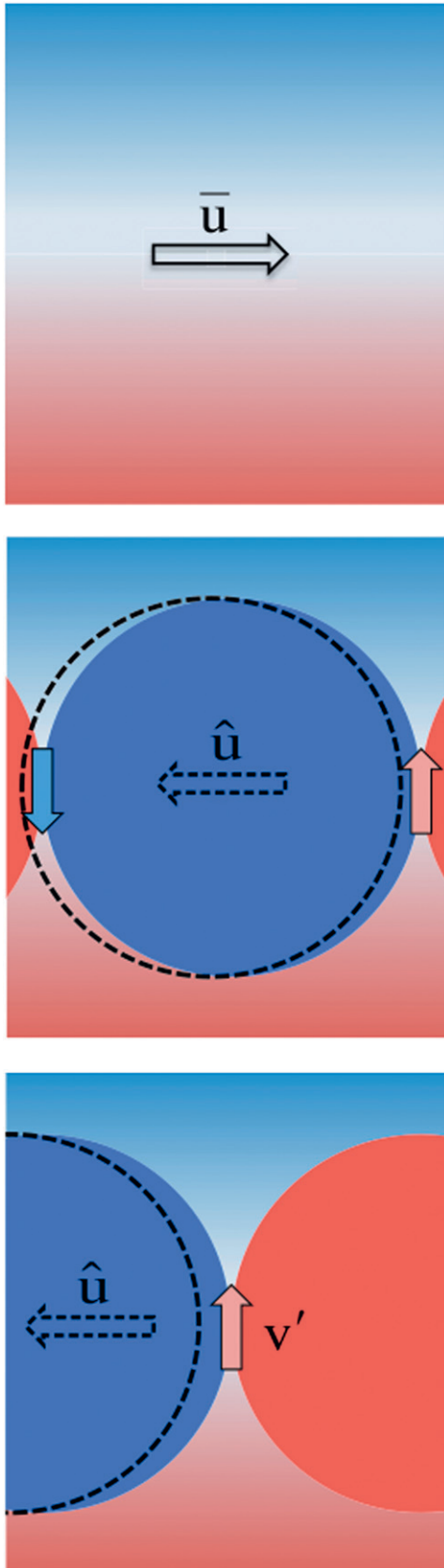
FIG. 3. The spatial structure of the least-damped eigenmode of the tangent linear mode: anomalies of (top) upper-ocean temperature and surface currents and (bottom) meridional streamfunction and zonally averaged temperature for phases (left) A and (right) B of the oscillation. During phase A, there exists a strong temperature anomaly in the northern Atlantic with a nonzero zonal mean, but the AMOC overturning anomaly is close to zero. During phase B, there develops a dipole-like temperature anomaly (with a zero zonal mean), associated with a strong AMOC anomaly. The two phases (A and B) are separated by a quarter-period or roughly 6 years. Temperature is given in terms of density. The upper-ocean temperature is averaged over the top 240 m. For the plot of streamfunction: solid, dashed, and dotted lines indicate positive, negative, and zero values, respectively; CI is 1 Sv. Anomalous velocities reach 6 cm s^{-1} . Note that all variables can be multiplied by an arbitrary factor since we consider a linear problem.

We should also emphasize that the eigenmode we describe is not driven by convection. In fact, the approximations of the tangent linear and adjoint models assume that tracer diffusivities are fixed, and so is the ocean mixed layer depth. Consequently all changes in the vertical flow are determined by divergence or convergence of the horizontal flow associated with large-scale density anomalies. Thus, our results confirm that AMOC variability can occur without changes in the mixed layer depth and hence convection. In general, one should distinguish vertical motion in the AMOC (a result of the horizontal flow divergence) and deep convection (sinking of water parcels that have a negative buoyancy anomaly). It has been shown that convection is a net sink of oceanic potential energy, rather than a source, and thus cannot maintain the AMOC (e.g., Wunsch and Ferrari 2004). Furthermore, a number of studies show that changes in

deep convection and the AMOC are not necessarily related (Marotzke and Scott 1999; de Boer et al. 2010). This is consistent with our results—changes in the AMOC intensity are driven not by changes in convection, but by changes in the pressure difference between the east and the west of the basin. This is not to say, however, that the interdecadal mode will not affect deep convection, but rather that changes in convection will be a next-order effect for the dynamics.

b. The biorthogonal mode

Using a similar mathematical procedure we have computed the least-damped eigenmodes $|\mathbf{u}_1^*|$ of the propagator of the adjoint model \mathbf{M}_1^* . This mode is defined as the biorthogonal to the least-damped eigenmode of the tangent linear propagator $|\mathbf{u}_1|$. That is, the biorthogonal mode or the adjoint eigenmode is orthogonal to every



eigenmode of the tangent linear propagator except $|\mathbf{u}_1\rangle$ (defining a contravariant projection). Since the system is nonnormal ($\mathbf{M}\mathbf{M}^\dagger - \mathbf{M}^\dagger\mathbf{M} \neq 0$), the least-damped mode of the tangent linear model and that of the adjoint differ from each other ($|\mathbf{u}_1\rangle \neq |\mathbf{u}_1^\dagger\rangle$). Because of the non-normality, we can expect a stronger temporal variability in the system when subjected to stochastic forcing (Ioannou 1995), which is associated with the efficient stimulation of the eigenmodes of the tangent linear model that would occur through the stimulation of the biorthogonal modes. This stems from the fact that, for instance, $|\mathbf{u}_1^\dagger\rangle$ has the biggest normalized covariant projection on $|\mathbf{u}_1\rangle$.

As expected, the least-damped mode of the adjoint has the same period and decay scale as that of the tangent linear (forward) model. However, the spatial structure of the adjoint mode is very different. It is important that temperature and salinity anomalies in the adjoint mode have a constructive effect on density, rather than compensating as in the tangent linear mode (see also Sévellec et al. 2009). The effect of salinity on density in the adjoint mode slightly dominates that of temperature. The adjoint mode is most pronounced in the deep ocean below 500 m northwest of the North Atlantic Current. (Figs. 8 and 9).

As mentioned before, the least-damped mode of the adjoint has the maximum covariant projection onto the least-damped mode of the forward model. Consequently, the former controls the sensitivity of the latter to initial perturbations. Thus, to understand the spatial structure of the biorthogonal mode, it is important to understand why specific changes in temperature or salinity in a particular region can stimulate efficiently the leading eigenmode of the forward model. In our case, temperature and salinity

←

FIG. 4. A schematic of the least-damped eigenmode showing the mechanism of the westward propagation of temperature anomalies. Blue and red represent the mean temperature distribution (light colors) and temperature anomalies in the upper ocean (heavier colors), respectively. (top) The background meridional temperature gradient and the corresponding eastward geostrophic flow \bar{u} . (middle) Phase A of the oscillation with a strong cold temperature anomaly but no change in the meridional overturning. (bottom) Phase B of the oscillation with a dipole temperature anomaly and a strong anomaly in the meridional overturning associated with the anomalous northward geostrophic flow v' in the upper ocean. The cold temperature anomaly in the middle panel induces cyclonic circulation in the ocean that transports cold water southward along the western flank of the anomaly and warm water northward along the eastern flank. This water transport results in the effective westward propagation of the original temperature anomaly with the equivalent velocity \hat{u} (geostrophic self-advection). The net of two velocities ($\hat{u} + \bar{u}$) is westward, as long as $|\hat{u}| > |\bar{u}|$. The β -effect contributes to the westward propagation as well.

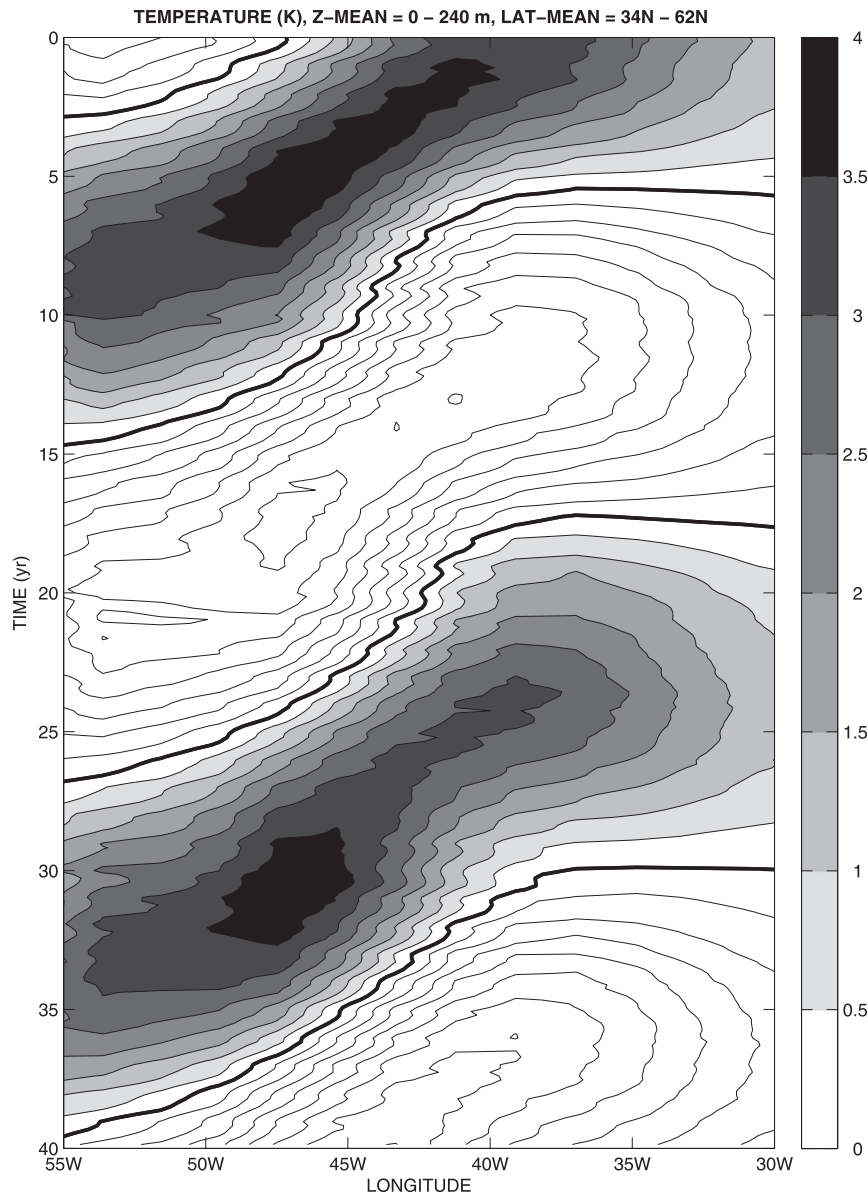


FIG. 5. A Hovmöller diagram showing westward propagation of temperature anomalies in the least-damped eigenmode. Temperature has been averaged over the upper 240 m in the latitudinal band 34°N to 62°N. Thick solid line corresponds to zero value. Gray-scale shading is used for positive values (following the colorbar). Contours without shading indicate negative values. The CI is 0.5K. The exponential decay of anomalies is suppressed.

anomalies of the biorthogonal mode are located predominantly in the part of the ocean where they can avoid propagation or deformation, which allows them to persist and impact ocean circulation most efficiently.

In fact, temperature and salinity anomalies of the biorthogonal mode are strongest in the region where ocean currents are weak (away from the NAC; Fig. 11, left, discussed in greater detail below) and at depths where horizontal density gradients nearly vanish and so does the possibility for westward propagation. Through

thermal wind balance such anomalies are able to create a persistent anomalous advection in the upper ocean and hence stimulate the least-damped mode of the forward model. The fact that the speed of propagation of temperature and salinity anomalies in the biorthogonal mode is very slow allows an efficient excitation of the interdecadal mode on long time scales, which partially explains the overall structure of the biorthogonal mode.

The constructive effect of temperature and salinity on density in the biorthogonal mode can be understood by

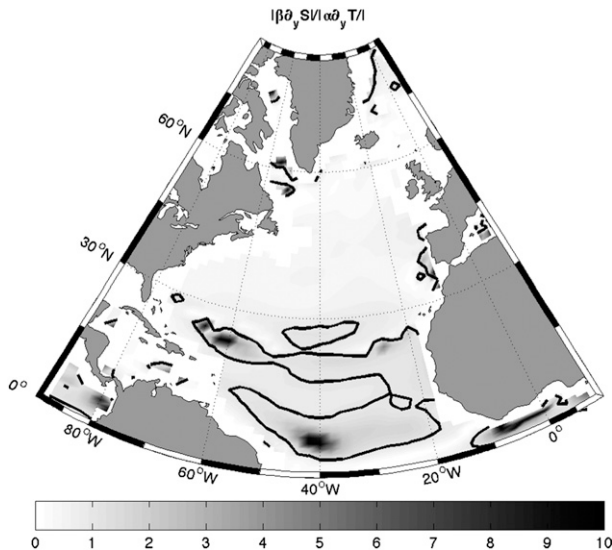


FIG. 6. The density ratio between meridional gradients of salinity and temperature averaged in the upper 500 m for the mean state produced by the full ocean GCM $|\beta \partial_y S'| / |\alpha \partial_y T'|$. The contour line corresponds to the ratio of 1.

the same logic. A constructive density anomaly will induce a greater anomalous velocity that will be more efficient in extracting temperature anomalies from the background temperature field, and thus more efficient in generating the least-damped mode of the tangent linear model.

To summarize, the stimulation of the eigenmode by its biorthogonal can be described by the following process: together, temperature and salinity anomalies of the biorthogonal pattern induce a strong geostrophic flow. In turn, this flow in the upper ocean extracts from the mean ocean state new anomalies in temperature and salinity. The new anomalies have opposite effects on density, but since the mean state is dominated by the meridional temperature gradient, density anomalies are now controlled largely by temperature. These density anomalies propagate westward and define the oscillatory eigenmode dominated by temperature and partially compensated by salinity.

4. The idealized model

a. Formulation

To better understand the oscillatory mechanism of the mode in the ocean GCM, we have formulated an idealized model that includes the essential linear dynamics of the oscillation and westward propagation.

The idealized model has only two levels in the vertical (Fig. 10) and invokes several key approximations. For simplicity, given the decadal time scale of the oscillation, we consider the system as autonomous (no seasonal cycle). Also, the large basin scale of the mode allows us to reduce the momentum equations to geostrophic

balance on a β plane (i.e., the planetary–geostrophic regime; Colin de Verdière 1988).

Given the dominant effect of temperature on density in the mode ($|\beta S'| \ll |\alpha T'|$, where T' and S' are temperature and salinity anomalies, respectively), at first we restrict the dynamics to temperature variations. Accordingly, the model describes anomalies in temperature at two levels—the top level (of depth h) and the deep level. We define the upper ocean as the part of the ocean with strong stratification, and the deep ocean as that with weak or no stratification. To simplify the mathematical procedure of the analysis, meridional variations in T' are neglected (anomalies are considered to be functions of time t and the zonal coordinate x). The zonal extent of the model ocean is W ; the full ocean depth is H .

In the absence of stratification in the deep ocean, we choose T' (temperature anomalies in the upper ocean) as prognostic variables of the model, where for simplicity we dropped the subscript u (upper). These anomalies evolve according to a linearized advective–diffusion equation with horizontal diffusivity κ :

$$\partial_t T' = -\bar{u} \partial_x T' - v' \partial_x \bar{T} - w' \partial_z \bar{T} + \partial_x (\kappa \partial_x T'), \quad (8)$$

where v' and w' are anomalous meridional and vertical velocities, respectively.

This equation is linearized with respect to the mean state of the ocean. In particular, at the upper level we impose a mean zonal flow \bar{u} and a mean temperature gradient. This gradient has meridional and vertical components: $\partial_y \bar{T}$ and $\partial_z \bar{T}$, where y and z are the meridional and vertical coordinates, and \bar{T} is a mean temperature. The mean zonal gradient of temperature is neglected. The values of the mean fields in (8) are given by simple constants estimated from the climatological run with the full ocean GCM.

In the ocean GCM, a horizontal Laplacian diffusivity is used with its value chosen to yield a realistic representation of the ocean-mean circulation and stratification (Madec et al. 1998). As we demonstrate in the idealized model, it is the value of diffusivity that controls the decay time scale of the eigenmode. In fact, using the same horizontal diffusivity in the idealized model as in the GCM produces the exact same damping scale for the leading eigenmode.

The system is closed using a linear equation of state for seawater, thermal wind balance for the meridional velocity with the baroclinicity condition applied, and the continuity equation for the anomalous flow:

$$\partial_z v' = \frac{\alpha g h}{f H} \partial_x T' \quad \text{with} \quad \int_{-H}^0 dz v' = 0 \quad \text{and} \quad (9a)$$

$$\partial_y v' + \partial_z w' = 0 \quad \text{with} \quad w'|_{z=0} = 0, \quad (9b)$$

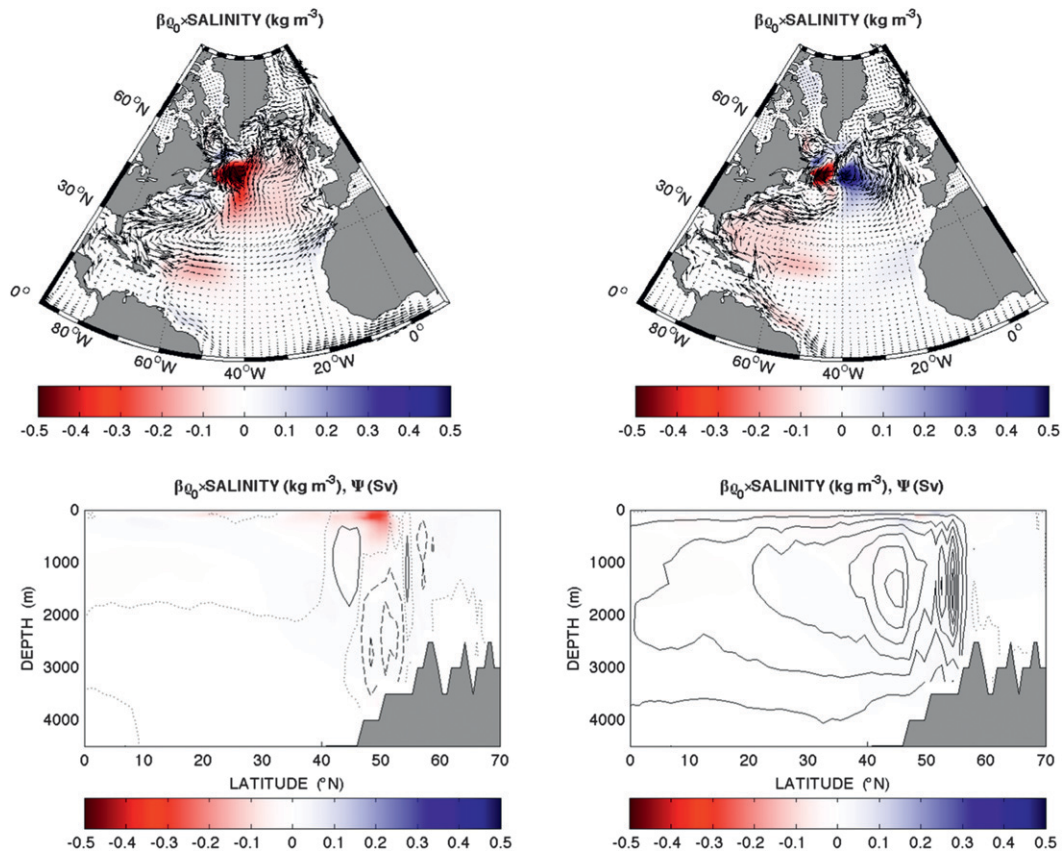


FIG. 7. As in Fig. 3, but for salinity variations.

where f is the Coriolis parameter and g is the acceleration of gravity (for the typical values of these parameters, see Table 1).

Using thermal wind balance, the baroclinicity condition, and considering ocean dynamics at the top and deep levels, we obtain a simple expression for the anomalous meridional velocity in the upper ocean:

$$v' = \frac{\alpha g h \tilde{h}}{2Hf} \partial_x T', \quad (10)$$

where $\tilde{h} = H - h$ is the thickness of the deep level. The divergence of this meridional flow will induce anomalous vertical velocity in the upper ocean. Setting w' to zero at the ocean surface, we obtain

$$w' = -\frac{\alpha g \tilde{h}^2 \beta_f}{4Hf^2} \partial_x T', \quad (11)$$

where $\beta_f = \partial_y f$ is the meridional gradient of planetary vorticity.

Using (8), (10), and (11), we reduce the dynamics of the idealized model at the upper level to one equation:

$$\partial_t T' = -c \partial_x T' + \kappa \partial_{xx} T', \quad (12)$$

where

$$c = \bar{u} + \hat{u} + c_{R0} \quad (13)$$

is the full speed of the mode propagation, with $\hat{u} = (\alpha g h \tilde{h} / 2Hf) \partial_y \bar{T}$ and $c_{R0} = (-\alpha g h \tilde{h}^2 \beta_f / 4Hf^2) \partial_z \bar{T}$. Here, \hat{u} is the equivalent speed of westward propagation of temperature anomalies on the background meridional temperature gradient (geostrophic self-advection, as sketched in Fig. 4). Note that c_{R0} represents the phase velocity of long (nondispersive) baroclinic Rossby waves caused by the β -effect, and \bar{u} describes the mean eastward flow. Simple estimates show that the Rossby wave propagation speed caused by the β -effect is significantly slower than the geostrophic self-advection ($c_{R0} < \hat{u}$) in mid to high latitudes.

Also, using the baroclinicity condition and the equation for v' in the upper ocean, we can compute variations in the meridional volume transport associated with temperature anomalies as

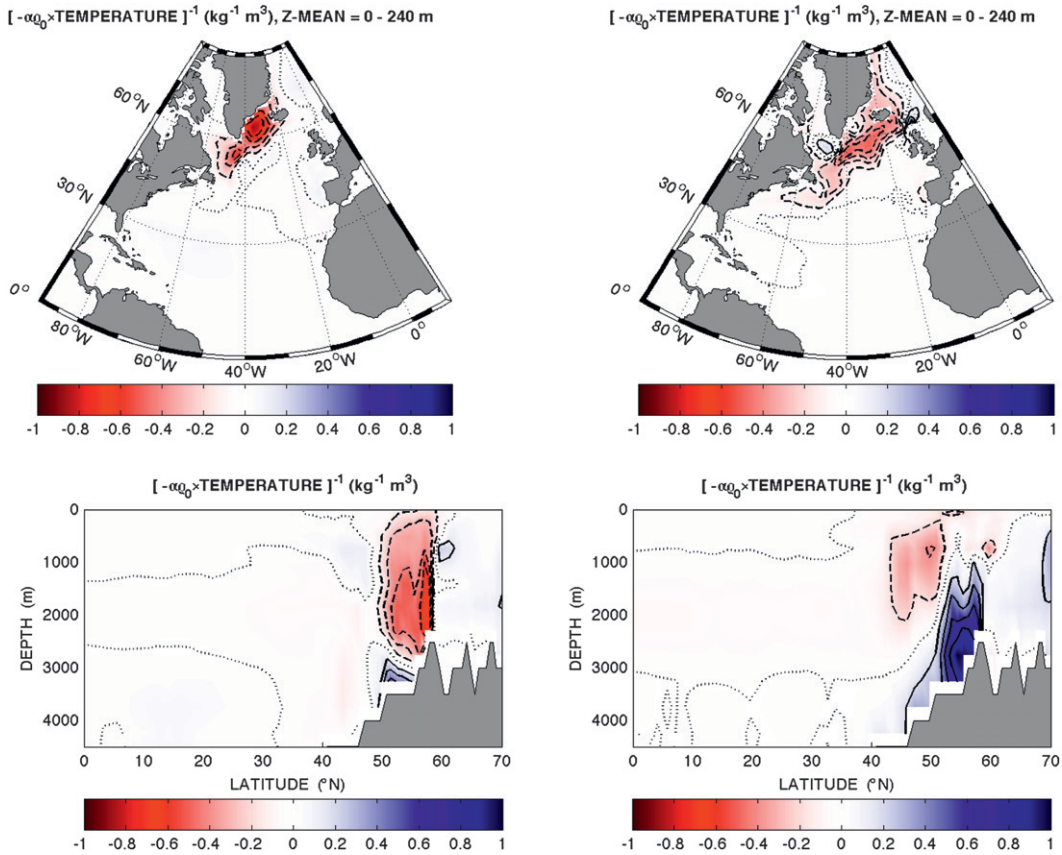


FIG. 8. As in Fig. 3 but for the least-damped eigenmode of the adjoint model (only for temperature component). Horizontal velocities and the meridional streamfunction are not shown.

$$\psi' = \int_{-h}^0 \int_0^W v' dx dz = (hW)V' = \frac{\alpha g \bar{h} h^2}{2Hf} (T'_{\text{West}} - T'_{\text{East}}), \quad (14)$$

where ψ' is the anomalous transport, V' is the zonally averaged meridional velocity, and T'_{West} and T'_{East} are temperature variations at the western and the eastern boundaries of the basin, respectively. We will use this equation in the next sections.

Further, we expand temperature anomaly T' into Fourier harmonics:

$$T' = \sum_n T_{cn} \cos\left(\frac{n\pi}{W}x\right) + T_{sn} \sin\left(\frac{n\pi}{W}x\right),$$

where n is the wavenumber.

Appropriate boundary conditions are still needed to supplement the advection–diffusion equation and constrain the problem. To obtain such conditions one would need to consider model dynamics near the basin boundaries, since the Fourier expansion is meant to describe the

interior solution of the problem where geostrophic balance can be applied (geostrophic balance filters Kelvin waves as well as short Rossby waves). Expression (14), connecting the streamfunction and temperature anomalies, is also based on the geostrophic approximation. To obtain a full solution of the problem one would need to introduce boundary layers connecting the geostrophic interior solution to the basin boundaries (for details see appendix A).

For the long decadal time scales, we consider that the basin boundary can be treated as being in a steady state (i.e., the east and west boundary layers are always adjusted). This assumption follows the demonstration of Johnson and Marshall (2002), for example, who showed that the basin boundary adjustment in the Atlantic occurs over 2–3 months and is largely completed by Kelvin waves propagating along the basin boundaries including the equator. We have tested whether this assumption holds in the ocean GCM and it appears that it does hold approximately (appendix A). For the idealized model, we can simply assume that the east and west boundary

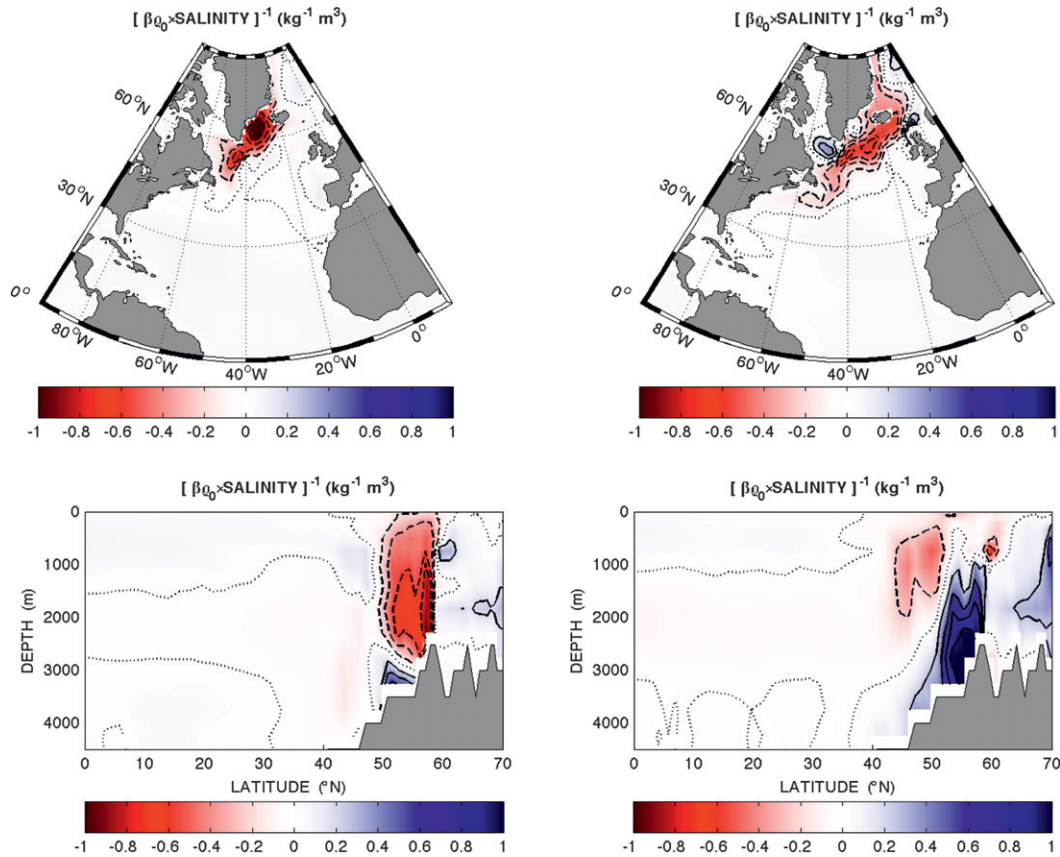


FIG. 9. As in Fig. 8, but for the salinity component of the least-damped eigenmode of the adjoint model.

layers are adjusted at all times together ($\partial_t \langle T \rangle_{\text{EB}} = \partial_t \langle T \rangle_{\text{WB}}$, where $\langle \cdot \rangle_{\text{EB}}$ and $\langle \cdot \rangle_{\text{WB}}$ denote 3D spatial averages for the east and west boundary layers, respectively). In other words, a warming/cooling in the east and west boundary layers should occur at the same time.

Using the temperature advection–diffusion equation and the aforementioned boundary layer dynamics, we show in appendix A that the appropriate boundary conditions for the interior solution become $\partial_x T'|_{\text{East}} = -\partial_x T'|_{\text{West}}$ and $T'_{\text{East}} = -T'_{\text{West}}$. In summary, they are a consequence of two factors: (i) the basin boundary is reset by Kelvin waves and (ii) the boundary layer dynamics are necessary to connect the geostrophic interior solution with the basin boundary. These boundary conditions restrict the solution to odd wavenumbers, which describe dipole-like temperature anomalies alternating with temperature anomalies centered in the middle of the basin (cf. Fig. 3) and allow for a continuous, albeit damped, oscillation.

The Fourier amplitudes T_{cn} and T_{sn} obey simple differential equations:

$$\partial_t T_{cn} = -c \frac{n\pi}{W} T_{sn} - \kappa \left(\frac{n\pi}{W} \right)^2 T_{cn} \quad \text{and} \quad (15a)$$

$$\partial_t T_{sn} = c \frac{n\pi}{W} T_{cn} - \kappa \left(\frac{n\pi}{W} \right)^2 T_{sn}. \quad (15b)$$

This system's complex conjugate eigenvalues are

$$\lambda_n^\pm = \lambda_{nr} \pm i\lambda_{ni} = -\kappa \left(\frac{n\pi}{W} \right)^2 \pm i \frac{n\pi}{W} c. \quad (16)$$

An estimate using ocean typical values from Table 1 gives for the gravest mode ($n = 1$) a period of $T = 2\pi/\lambda_{li} = 5.2$ yr and an e -folding decay time scale of $\tau = 1/\lambda_{lr} = -36.1$ yr. The corresponding eigenvectors are

$$|\mathbf{u}_n^\pm\rangle = \frac{\sqrt{2}}{2} \begin{pmatrix} \pm i \\ 1 \end{pmatrix}.$$

We will demonstrate in the next sections that the relatively short period given by (16) becomes significantly longer and comparable to that in the ocean GCM

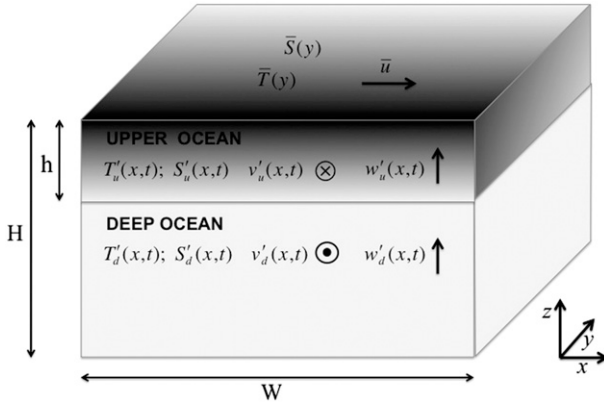


FIG. 10. A schematic of the idealized model (cf. Fig. 4). The two levels of the model represent the upper and deep ocean, respectively. The model four prognostic variables are temperature and salinity in the upper and deep ocean (T'_u , S'_u , T'_d , and S'_d , respectively). The four diagnostic variables are meridional velocities in the upper and deep ocean (v'_u and v'_d , respectively), and the vertical velocity in the upper and deep ocean (w'_u and w'_d , respectively). The main model parameters are the upper ocean thickness h , the total ocean depth H , the zonal extent of the Atlantic basin W , and the mean meridional flow \bar{u} and temperature and salinity fields in the upper ocean (\bar{T} and \bar{S} , respectively). The intensity of the shading (lighter to darker) represents the spatial variation of the mean temperature (cooler to warmer). In the upper ocean, we use a linear function of y . In the deep ocean, we use constant values equal to temperature at the northern basin boundary of the upper ocean. Also, we implicitly assumed that there is a nonzero vertical temperature gradient in the upper layer that can support baroclinic Rossby waves due to the β -effect. The dependency of the model variables from space coordinates (zonal- x , meridional- y , and vertical- z) and time t is shown in brackets.

if the effect of the meridional salinity gradient on density is taken into account.

b. The mode oscillatory mechanism and nonnormality

The idealized model and its eigenvectors confirm that the system can exhibit a damped oscillation in which temperature anomalies propagate westward (as long as the meridional gradient of temperature is strong enough to maintain the westward propagation tendency against the mean flow). The oscillation goes through quadrature phases (corresponding to the cosine and sine in the expression for T'). The first phase is characterized by an anomaly in the zonally averaged temperature (proportional to the sine with $n = 1$) and no change in meridional streamfunction (14), whereas the second phase is characterized by an anomaly in the zonal temperature gradient (proportional to the cosine with $n = 1$) and a corresponding anomaly in the meridional overturning (14). Thus, the oscillation in the idealized model undergoes exactly the same phases as the least-damped

TABLE 1. Typical parameters used in the idealized model.

h	1200 m	Upper layer thickness
H	4500 m	Total ocean depth
W	60°	Zonal basin size
L	60°	Meridional basin size
κ	$2 \times 10^3 \text{ m}^2 \text{ s}^{-1}$	Horizontal tracer diffusivity
g	9.8 m s^{-2}	Acceleration caused by gravity
f	10^{-4} s^{-1}	Coriolis parameter
β_f	$1.5 \times 10^{11} \text{ m}^{-11} \text{ s}^{-1}$	β -effect (the gradient of planetary vorticity)
α	$2 \times 10^{-4} \text{ K}^{-1}$	Thermal expansion coefficient
β	$7 \times 10^{-4} \text{ psu}^{-1}$	Haline contraction coefficient
ΔT	-15 K	Mean meridional temperature contrast
ΔS	-1.5 psu	Mean meridional salinity contrast
\bar{u}	$2.5 \times 10^{-2} \text{ m s}^{-1}$	Mean zonal velocity in the upper ocean

mode of the tangent linear GCM—the phases characterized by anomalies in the zonally averaged temperature followed by anomalies in the AMOC a quarter-period later (see Fig. 2).

1) THE ROLE OF WAVENUMBER

According to expression (16), both the oscillation period and the e -folding decay time scale of different modes in the idealized model depend on wavenumber. In fact, the period is given by the inverse of wavenumber, while the decay time scale is given by the inverse of wavenumber squared. Therefore, modes with $n \geq 3$ are more strongly damped by dissipative processes than the gravest mode (with $n = 1$). This explains why the mode with the smallest wavenumber is least damped in the system.

2) THE ROLE OF MEAN ZONAL VELOCITY

To evaluate the importance of the mean eastward advection \bar{u} , we can compare it with the equivalent zonal velocity caused by the mean meridional temperature gradient $\hat{u} = (\alpha g h \bar{h} / 2 H f) \partial_y \bar{T}$. This equivalent zonal velocity is westward as long as temperature decreases with latitude, and simple estimates (using parameters from Table 1) show that its magnitude exceeds the eastward tendency of the mean zonal flow (Fig. 11). The β -effect increases the westward tendency even further. Thus, temperature anomalies will indeed propagate westward in accordance with the mechanism described in Fig. 4 (also see Table 2)—that is, the geostrophic self-advection caused by the background meridional temperature gradient. This gradient is strongest in the northern Atlantic, between 30° and 60°N, which explains the predominant location of the oscillatory mode. Although the mean eastward advection is not needed for the oscillatory mechanism, it is still important in computing the period

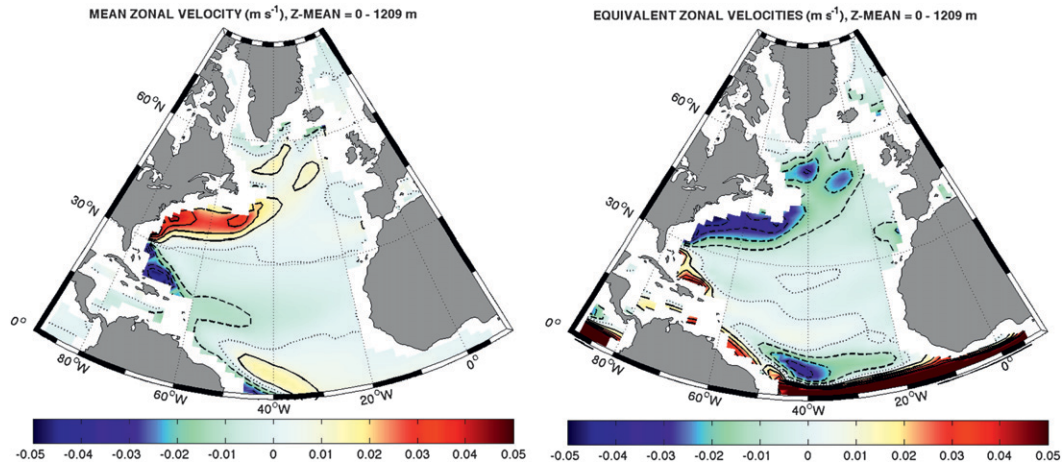


FIG. 11. (left) Mean zonal velocity in the upper ocean. (right) Equivalent zonal velocity in the upper ocean calculated as $(ghh/2Hf)(\alpha\partial_y T - \beta\partial_y S)$. The fields are produced by the full ocean GCM. Note that the β -effect also contributes to westward propagation.

of the mode accurately (Fig. 12) as described in the next sections.

Note that in very idealized settings, in which both the mean flow and its perturbations are described solely by the first vertical baroclinic mode as in the $1\frac{1}{2}$ -layer shallow-water equations, the geostrophic self-advection of temperature anomalies and advection by the mean flow would cancel each other, resulting in westward propagation controlled exclusively by the β -effect. This cancellation is known as the non-Doppler effect (Rossby et al. 1939; Held 1983; Killworth et al. 1997).

3) THE ROLE OF THE DEEP OCEAN

Other important effects, not critical for the existence of the mode but affecting its period and non-normal dynamics, include salinity and the influence of the deep ocean. For example, as we showed in section 3b, the biorthogonal to the least-damped oscillatory mode of the linearized GCM has a stronger signature below 1000 m than at the surface (Figs. 8 and 9, section 3b).

To include the effect of the deep ocean in the idealized model, we need to modify (15). This can be done by adding to the system two new equations for the Fourier amplitudes of the deep ocean temperature T_{cn}^d and T_{sn}^d (appendix B). A linear stability analysis of the new system yields four eigenvalues:

$$\lambda_{1,2} = -\kappa \left(\frac{n\pi}{W} \right)^2 \pm i \frac{n\pi}{W} c \quad \text{and} \quad \lambda_{3,4} = -\kappa \left(\frac{n\pi}{W} \right)^2, \quad (17)$$

where still $c = \bar{u} + \hat{u} + c_{R0}$, with $\hat{u} = (\alpha g h \tilde{h} / 2 H f) \partial_y \bar{T}$ and $c_{R0} = (-\alpha g h \tilde{h}^2 \beta_f / 4 H f^2) \partial_z \bar{T}$.

The first two (oscillatory) eigenvalues of the system $\lambda_{1,2}$ have not changed. The last two components of the

corresponding eigenvectors are zero, so that in agreement with the tangent linear GCM (Figs. 3 and 7) the deep ocean does not affect the leading mode of the system directly.

The new eigenvalues $\lambda_{3,4}$ are degenerate and describe a purely decaying mode with an e -folding decay time scale of approximately 36 yr. This mode also has a strong signature in the upper ocean.

We can examine the sensitivity of the eigenvectors (i.e., find the most efficient patterns to excite them) by computing their biorthogonals, see (B4) in appendix B. It turns out that, although the dynamics of the two damped modes $|\mathbf{u}_3\rangle$ and $|\mathbf{u}_4\rangle$ are mainly controlled by the upper ocean, their sensitivities, $|\mathbf{u}_3^\dagger\rangle$ and $|\mathbf{u}_4^\dagger\rangle$, are controlled solely by the deep ocean. The sensitivity of the oscillatory mode $|\mathbf{u}_{1,2}^\dagger\rangle$ is also largely controlled by the deep ocean. Such asymmetry between the eigenvectors and their biorthogonals is a consequence of the non-normality of the system dynamics.

These results are consistent with the analysis of the ocean GCM (section 3). That is, the deep ocean is a critical region for the sensitivity of the oscillatory mode,

TABLE 2. The period and e -folding decay time scale of the interdecadal oscillation obtained from expression (18) with $n = 1$ for the idealized model with different combinations of the mean meridional salinity contrast and zonal velocity. Appropriate nonzero values are taken from Table 1.

Model	Period II	Decay τ
Tangent linear GCM	24.0 yr	-40.0 yr
Idealized model:		
$\partial_{y,z} S = 0, \bar{u} = 0$	5.2 yr	-36.1 yr
$\partial_{y,z} S = 0, \bar{u} \neq 0$	8.0 yr	-36.1 yr
$\partial_{y,z} S \neq 0, \bar{u} = 0$	9.1 yr	-36.1 yr
$\partial_{y,z} S \neq 0, \bar{u} \neq 0$	23.8 yr	-36.1 yr

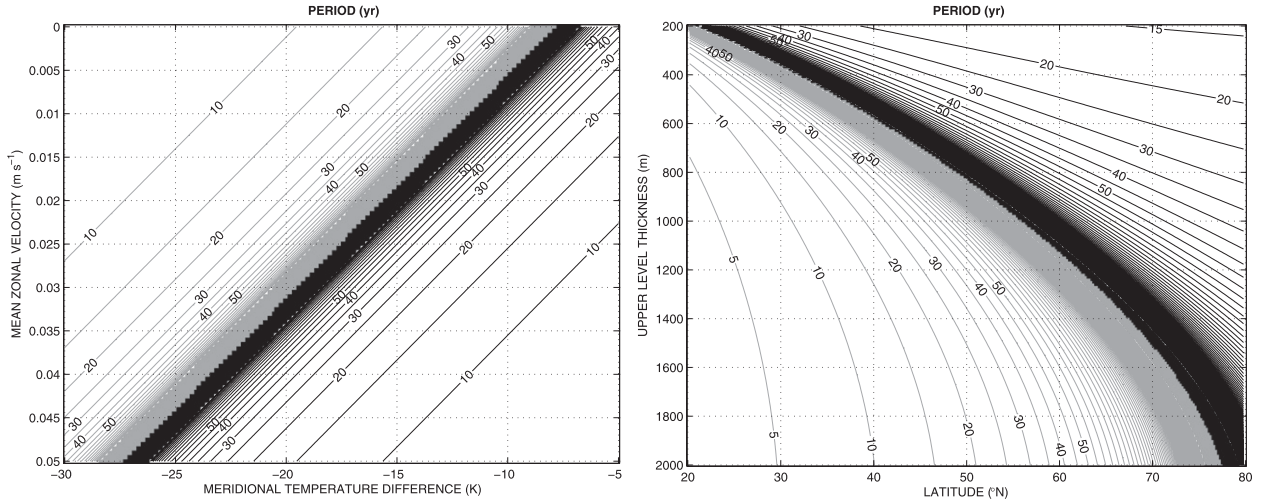


FIG. 12. The period of the interdecadal mode in the idealized model, obtained from expression (18) with $n = 1$. The CI is 5 yr; gray and black lines indicate westward and eastward propagation, respectively. Along the boundary between black and gray lines the period becomes infinite.

even though the mode manifests itself in the upper ocean. This is because temperature anomalies persist longer in the deep ocean (where both mean currents and geostrophic self-advection are weak) and can excite the oscillatory mode more efficiently.

4) THE ROLE OF THE SALINITY

Another important factor that can influence the properties of the leading oscillatory eigenmode and its sensitivity involves salinity. Using the tangent linear GCM and its adjoint (section 3), we have shown that the oscillation dynamics are largely controlled by temperature variations in the upper ocean (with salinity having a compensating effect on density). However, the sensitivity of the oscillation (i.e., the biorthogonal mode) is almost controlled equally by temperature and salinity (with the two now having a constructive effect on density). These results are related again to the nonnormality of the system associated with the different effects on density of the mean temperature and salinity gradients in the northern Atlantic.

Here, we examine these results by extending the idealized model described by (15) to include salinity variations (but not the effect of the deep ocean). To that end, we introduce S_{cn} and S_{sn} —the Fourier amplitudes for the upper-ocean salinity (similar to T_{cn} and T_{sn}), which will add two more equations to system (15) (for details, see appendix C).

A linear stability analysis of the new equations yields four eigenvalues:

$$\lambda_{1,2} = -\kappa \left(\frac{n\pi}{W} \right)^2 \pm i \frac{n\pi}{W} c \quad \text{and} \quad \lambda_{3,4} = -\kappa \left(\frac{n\pi}{W} \right)^2 \pm i \frac{n\pi}{W} \bar{u}, \quad (18)$$

where $c = \bar{u} + \hat{u} + c_{R0}$, but now $\hat{u} = (gh\tilde{h}/2Hf)(\alpha\partial_y\bar{T} - \beta\partial_y\bar{S})$ and $c_{R0} = (ghh^2\beta_f/4Hf^2)(-\alpha\partial_z\bar{T} + \beta\partial_z\bar{S})$.

The first two eigenvalues $\lambda_{1,2}$ and the corresponding eigenvectors are similar to those in the temperature-only model, but with the speed of westward propagation modified to include mean meridional and vertical salinity variations. The oscillation is still dominated by temperature and the mode dynamics are described by the westward propagation of density anomalies as long as $|\alpha\partial_y\bar{T}| > |\beta\partial_y\bar{S}|$, which holds well in the northern Atlantic (Fig. 11). However, the speed of westward geostrophic self-advection decreases because of the reduction of the mean meridional density gradient caused by salinity. Note that in the absence of the mean meridional temperature gradient the propagation of density anomalies would be eastward.

Estimating the period and the e -folding decay time scale of the leading oscillatory mode for the typical parameters in Table 1 and $n = 1$ gives $2\pi/\Im(\lambda_{1,2}) = 23.8$ yr for the period and $1/\Re(\lambda_{1,2}) = -36$ yr for the decay scale (\Re and \Im denote real and imaginary parts, respectively), which agrees well with the ocean GCM results.

The other two eigenvalues $\lambda_{3,4}$ and the corresponding eigenvectors represent a mode passively advected by the mean currents and damped by diffusion. It is a spiciness mode with eastward propagation (a spiciness anomaly does not modify density and hence cannot experience geostrophic self-advection). The period of this mode is 12 yr for the mean current of 2.5 cm s^{-1} , and its decay time scale is -36 yr.

As previously, differences between the mode dynamics and its sensitivity become apparent when we compare the eigenmodes and their biorthogonals (C4a). The biorthogonals show that the passively advected mode

$|\mathbf{u}_{3,4})$ is more sensitive to salinity than to temperature variations, even though the mode itself does not have any preferences between the two fields in its dynamics (since it is a spiciness mode). For the oscillatory mode $|\mathbf{u}_{1,2})$, the biorthogonals show constructive patterns of temperature and salinity without a dominant term, even though the eigenmode itself is controlled by temperature anomalies only partially compensated by salinity. These results are similar to the GCM analysis (section 3), which again highlights that the ocean dynamics are nonnormal. Here, the cause of nonnormality is the asymmetry between mean temperature and salinity fields.

c. The mode period

We can now return to the question of what controls the period of the interdecadal eigenmode. Ultimately, this period is inversely proportional to c and is approximately equal to the time needed for a temperature (or density) anomaly to cross twice the northern Atlantic. Our study points to several key factors that determine this crossing time, including the meridional gradients of temperature and salinity, the mean zonal velocity, and the width of the basin (the latter parameter, along with horizontal diffusivity, also controls the mode decay time scale). As previously discussed, the meridional salinity gradient and the mean zonal flow, although not critical for the oscillation, are indeed important for setting the period of the mode. By slowing down the westward propagation, these two factors lengthen the oscillation period (Table 2).

To further understand the sensitivity of the mode period to different processes in the idealized model, we varied four parameters in (18): the mean zonal velocity (from 0 to 0.05 m s^{-1}), the meridional temperature contrast (from -30 to -5 K), the prevailing latitude at which temperature anomalies propagate (from 20° to 80°N), and the ocean upper layer thickness (from 200 to 2000 m).

Analyzing the sensitivity of the mode to the mean zonal velocity and the meridional temperature gradient reveals two different regimes (Fig. 12, left panel), with westward or eastward propagation. Which regime is achieved depends on whether the eastward flow is strong enough to overcome the westward tendency of the geostrophic self-advection and the β -effect. At the border between the two regimes the mode period goes to infinity (which corresponds to the zero propagation speed) and the oscillation degenerates into a purely damped mode.

The oscillation period also changes when the upper-level thickness, h in (18), is modified. Decreasing this thickness in the idealized model leads to a slower westward propagation speed and longer periods (before the direction of propagation changes sign) (see Fig. 12, right

panel). A similar effect occurs when we shift to higher latitudes at which density anomalies propagate (which modifies both the Coriolis parameter and the β -effect).

5. Conclusions

Ocean circulation can generate climate variability on a variety of time scales. In this study, we have conducted a stability analysis of a linearized version of a realistic ocean GCM and its adjoint and identified the leading (least damped) interdecadal eigenmode of the Atlantic meridional overturning circulation. The mode is associated with large-scale westward propagating density anomalies dominated by temperature but partially compensated by salinity. These temperature anomalies are most pronounced in the upper ocean of the North Atlantic in the band between 30° and 60°N where the mean meridional gradient of temperature is especially strong. In our model, this mode has a period of 24 yr and an e -folding decay time scale of roughly 40 yr. The damping increases severalfold if the surface mixed boundary conditions with a temperature restoring are applied instead of the flux boundary conditions (Sévellec and Fedorov 2013, manuscript submitted to *Prog. Oceanogr.*).

The westward propagation of temperature anomalies is largely explained by the geostrophic self-advection of the anomalies on the background of the mean meridional temperature gradient. Since the meridional salinity gradient in the North Atlantic mainly opposes that in temperature, the effect of salinity is to slow down the westward propagation. Two other factors determining the propagation characteristics are the β -effect (as in conventional Rossby waves) and the mean eastward flow. In general, the propagating temperature anomalies can be interpreted as planetary waves associated with a background vorticity gradient (controlled by meridional variations in density and planetary vorticity) and affected by mean currents. The period of the mode is determined by the time necessary for the temperature anomalies to cross the northern Atlantic.

An idealized two-level model, based on planetary-geostrophic equations for temperature and salinity anomalies (e.g., Colin de Verdière 1988), captures the main properties of the mode and emphasizes the importance of the mean meridional temperature gradient in the upper ocean for the mode dynamics. The meridional salinity gradient, while not critical for the mode mechanism, is still important for the oscillation period. The damping of the eigenmodes, according to the idealized model, is determined by horizontal diffusion. Consequently, the least-damped mode is the one with the smallest wavenumber and the greatest horizontal spatial scale. Other modes have shorter decay time scales,

so that asymptotically for a long time only the large-scale interdecadal mode survives.

The eigenmode described in our study can explain the westward propagation of depth-averaged temperature anomalies on decadal time scales as detected in the observations (e.g., Kushnir 1994; Frankcombe et al. 2008). The eigenmode spatial characteristics (i.e., alternation between temperature anomalies with a nonzero zonal mean and dipole-like temperature anomalies) and temporal behavior (a 20–30-yr period) are particularly consistent with the study of Frankcombe and Dijkstra (2009).

This eigenmode can also explain other properties of interdecadal variability highlighted in previous studies with comprehensive, intermediate-complexity, and simple climate models. For example, te Raa and Dijkstra (2002) discussed an oscillation that involved both meridional and zonal overturning circulations (ZOCs) in the Atlantic. In our model, the phase of the oscillation associated with the AMOC intensification corresponds to the thermocline shoaling in the west and deepening in the east, which is a signature of a strengthening of the ZOC.

Other examples include explanations of AMOC variability that involve changes in the subpolar or subtropical gyres and the upper-ocean heat content in the northern Atlantic (e.g., Dong and Sutton 2005; D'Orgeville and Peltier 2009; Danabasoglu 2008; Cheng et al. 2004). In our model both gyres are affected by anomalous currents associated with the large-scale temperature anomalies (Fig. 3) and hence anomalies in the upper-ocean heat content. Whereas the greatest changes in the gyre circulations occur when the total heat content of the upper northern Atlantic is either maximal or minimum, AMOC anomalies are strongest when heat content anomalies are weak (Fig. 2). Thus, our interdecadal eigenmode can account for the previously noted features of interdecadal variability in other ocean and climate models.

To better understand the properties of the system we have also examined the biorthogonal of the leading eigenmode (i.e., the least-damped eigenmode of the adjoint model). This “adjoint” mode describes the sensitivity of the leading “forward” mode; that is, it shows which regions of the ocean and which variables (temperature or salinity) should be perturbed to excite the forward mode. In other words, the adjoint mode gives the most efficient pattern to perturb the system, while the forward mode describes the asymptotic limit of a long time.

Because the system is nonnormal, the structure of the adjoint mode (the biorthogonal) is dramatically different from that of the forward mode. For example, temperature and salinity have opposite effects on density in the forward eigenmode but constructive in the adjoint

mode. The forward mode has the greatest signature in the upper ocean but the adjoint mode is more prominent in the deep ocean (where the mean flow and mean temperature and salinity gradients are at a minimum). These differences imply that standard statistical analyses used for studying AMOC variations may give misleading results when interpreting the properties of the leading eigenmode, because asymptotic characteristics of interdecadal variability can differ from those obtained from assessing short-term correlations.

As outlined by the idealized model, the nonnormality of the system is related to several factors leading to asymmetry in the linear prognostic equations. These factors include a significantly stronger stratification in the upper ocean than in the deep ocean, and the competition between the meridional gradients of temperature and of salinity in setting the meridional density gradient in the North Atlantic.

Several questions have not been yet addressed by this work. Even though the nonnormal properties of the oscillatory mode have been highlighted, we have not explored how atmospheric noise can excite this mode. As suggested by Ioannou (1995), the nonnormality should enhance the response of the AMOC to external perturbations. Another question is the robustness of the mode to changes in the surface boundary conditions. A new set of experiments (not shown) reveals that the mode can still exist for different boundary conditions (temperature restoring instead of constant heat fluxes). As expected, the leading eigenmode becomes more damped but retains its major properties, including the same oscillation period. Also, the sensitivity of the mode to surface salinity perturbations becomes enhanced relative to temperature perturbations (Sévellec and Fedorov 2013, manuscript submitted to *Prog. Oceanogr.*), which could be crucial for sustaining the mode by atmospheric synoptic noise.

Another issue not addressed in this study is the role of mesoscale eddies. In ocean models such as the one we use, turbulent mixing is represented by the Gent–McWilliams advection (Gent and McWilliams 1990) and by diapycnal and isopycnal diffusion. Mesoscale eddies (Chelton et al. 2007) as well as the low-frequency variability associated with the eddying ocean dynamics (e.g., Berloff and McWilliams 1999) are missing in the model. Given typical spatial scales of these eddies (~ 100 km), they are filtered out from spatially integrated temperature indices such as the AMO index for example (SSTs averaged over the North Atlantic). However, it is clear that mesoscale eddies should be considered in future work as a potential source of oceanic internal noise and a possible contributor to low-frequency variability.

Another important issue is the effect of ocean–atmosphere interactions on the interdecadal mode. In

particular, a series of studies have shown the importance of the thermal feedback on wind stress for generating or sustaining decadal variability (Cessi 2000; Gallego and Cessi 2000; Cessi and Paparella 2001). Preliminary results from the IPSL coupled climate model (a model that has OPA as its oceanic component) reveal a robust 20-yr interdecadal variability of the AMOC with dynamics apparently similar to those discussed in this study (Escudier et al. 2013). Atlantic Ocean variability in a coupled model with a simplified atmosphere and idealized continental geometry also resembles our mode (Buckley et al. 2012). The nonnormal excitation of the interdecadal mode (Sévellec and Fedorov 2013, manuscript submitted to *Prog. Oceanogr.*) and the role of coupled feedbacks are among the topics of ongoing and future work.

Acknowledgments. This research was supported by grants from the National Science Foundation Division of Ocean Sciences (NSF OCE-0901921), U.S. Department of Energy (DOE) Office of Science (DE-FG02-08ER64590, DE-SC0007037), the David and Lucile Packard Foundation, and the Ti Ammo project funded through the French Centre National de la Recherche Scientifique/ Institut National des Sciences de l'Univers/Les Enveloppes Fluides et l'Environnement (CNRS/INSU/LEFE) program. FS thanks Thierry Huck and Alain Colin de Verdière for useful comments on an early version of the manuscript. AVF thanks Peter Rhines and Igor Kamenkovich for a helpful discussion. We thank Rémi Tailleux, François W. Primeau, and two anonymous reviewers for help in improving the paper.

APPENDIX A

Boundary Conditions for the Idealized Model

Here, we derive the proper form of the boundary conditions for the idealized model. To do so, we need to introduce boundary layers into the problem. By itself, the idealized model describes only the interior solution of the problem, and the boundary layers are necessary to connect the interior flow to the basin boundaries.

To conform to the setup of the idealized model, we introduce two boundary layers (of thickness δ) at the western and the eastern sides of the basin (Fig. A1). We will assume that geostrophy is achieved at the outer edge of the boundary layers and the interior geostrophic flow slips freely along the edge. We will also assume that the two boundary layers are coupled at all times, adjusting together to perturbations. This latter assumption is consistent with the results of Johnson and Marshall (2002) and with the behavior of the ocean GCM. Indeed,

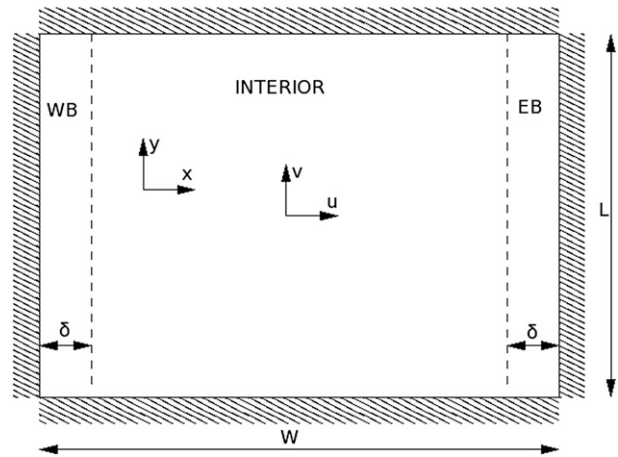


FIG. A1. The basin of the idealized model with the boundary layers set at the western and eastern sides (WB and EB, respectively). Here, W denotes the basin width.

Fig. A2 shows that average temperatures on the western and eastern sides of the North Atlantic in the model vary nearly in unison.

To formulate the boundary conditions, we start from the general advection–diffusion equation for temperature:

$$\partial_t T = -\partial_x(uT) - \partial_y(vT) - \partial_z(wT) + \partial_x k_x \partial_x T + \partial_y k_y \partial_y T + \partial_z k_z \partial_z T,$$

where z , x , and y are the vertical, zonal, and meridional coordinates (Fig. A1); w , u , and v are the vertical, zonal, and meridional velocities; and k_z , k_x , and k_y the vertical, zonal, and meridional diffusivities, respectively. For the sake of simplicity, we make the horizontal diffusion coefficients constant and equal to k_h .

After vertical and meridional integrations, with the assumption of zero heat flux at the ocean surface $k_z \partial_z T|_{z=0} = 0$, the advection–diffusion equation reduces to

$$\partial_t \langle T \rangle_{z,y} = -\partial_x \langle uT \rangle_{z,y} + k_h \partial_x^2 \langle T \rangle_{z,y}, \quad (\text{A1})$$

where $\langle T \rangle_{z,y} = \int_{-H}^0 \int_0^L T dy dz$ represents a spatial average of T over z and y .

We also use the nondivergence of the velocities field:

$$\partial_x v + \partial_y v + \partial_z w = 0.$$

After vertical and meridional integrations this equation becomes $\partial_x \langle u \rangle_{z,y} = 0$. Integrating from the outer edge of the western boundary layer to the outer edge of the eastern boundary layer, we obtain $\langle u|_{\delta} \rangle_{z,y} = \langle u|_{W-\delta} \rangle_{z,y}$.

Thermal wind balance together with the free slip condition $\partial_x v|_{\delta} = \partial_x v|_{W-\delta} = 0$ yields $\partial_x^2 T = 0$ at the outer

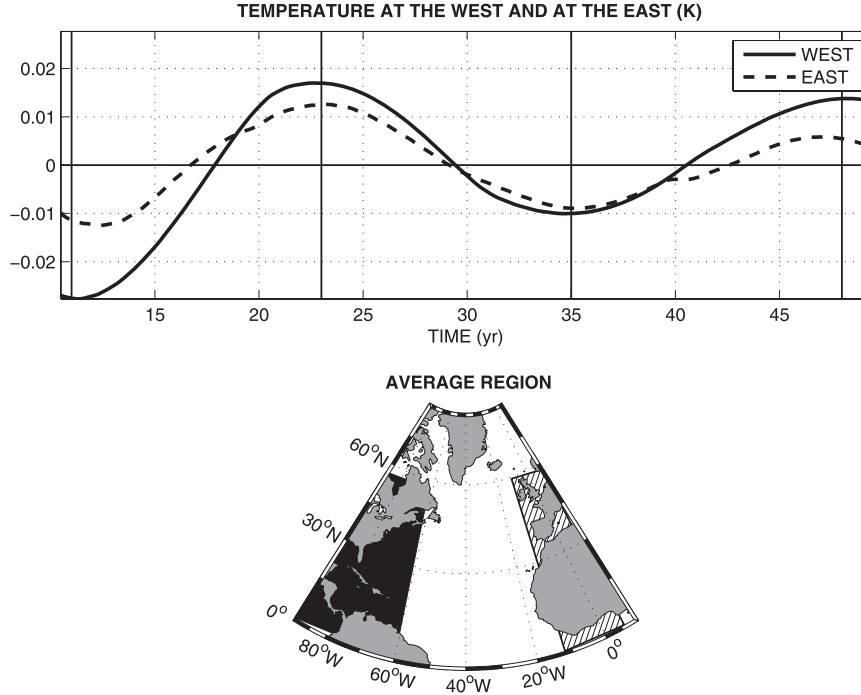


FIG. A2. (top) Temperature variations averaged over the western and eastern parts of the North Atlantic basin (solid and dashed lines, respectively). The east and west temperatures evolve in unison. (bottom) The regions of averaging for the time series shown at top. The zonal extent of the two regions is chosen to avoid the geostrophic interior region. The meridional extent is chosen to include the full meridional scale of the mode and minimize the relative heat and mass loss through the northern and southern boundaries.

edge of the boundary layers; therefore, along the border between the boundary layers and the interior flow we can neglect the second term of the right-hand side of (A1).

Adding the equations for integrated temperature at the outer edge of each boundary layers, and applying the results from the flow nondivergence, we obtain

$$\partial_t \langle T \rangle_{\delta, z, y} + \langle T \rangle_{W-\delta, z, y} = -\langle u \rangle_{\delta, z, y} \langle \partial_x T \rangle_{\delta, z, y} - \langle \partial_x T \rangle_{W-\delta, z, y} \quad (A2)$$

Returning to (A1) and integrating it zonally over the western and eastern boundary layers, with the assumption of zero heat flux at the solid boundaries, we obtain that the integrated boundary layer temperatures evolve as

$$\partial_t \langle T \rangle_{WB} = -\langle (uT) \rangle_{\delta, z, y} + k_h \langle \partial_x T \rangle_{\delta, z, y} \quad \text{and}$$

$$\partial_t \langle T \rangle_{EB} = \langle (uT) \rangle_{W-\delta, z, y} - k_h \langle \partial_x T \rangle_{W-\delta, z, y},$$

where $\langle T \rangle_{WB} = \int_0^{\delta} \langle T \rangle_{z, y} dx$ and $\langle T \rangle_{EB} = \int_{W-\delta}^W \langle T \rangle_{z, y} dx$.

Now assuming that the two boundaries adjust together and $\partial_t \langle T \rangle_{WB} = \partial_t \langle T \rangle_{EB}$, and again applying the flow nondivergence, we obtain

$$\langle u \rangle_{\delta, z, y} \langle T \rangle_{\delta, z, y} + \langle T \rangle_{W-\delta, z, y} = k_h \langle \partial_x T \rangle_{\delta, z, y} + \langle \partial_x T \rangle_{W-\delta, z, y}. \quad (A3)$$

In the context of the idealized model, (A2) and (A3) become

$$d_t (T'_{West} + T'_{East}) = -u_{West} (\partial_x T'|_{West} + \partial_x T'|_{East}) \quad \text{and} \quad (A4a)$$

$$u_{West} (T'_{West} + T'_{East}) = k_h (\partial_x T'|_{West} + \partial_x T'|_{East}), \quad (A4b)$$

where the subscripts West and East refer to the western and eastern boundaries of the interior geostrophic region.

Combining these two equations, we arrive at

$$d_t(T'_{\text{West}} + T'_{\text{East}}) = -\frac{u_{\text{West}}^2}{k_h}(T'_{\text{West}} + T'_{\text{East}}). \quad (\text{A5})$$

Time integrating (A5) yields

$$T'_{\text{West}}(t) + T'_{\text{East}}(t) = e^{-(u_w^2/k_h)t}[T'_{\text{West}}(0) + T'_{\text{East}}(0)].$$

This means that for sufficiently long times (at which the two boundary layers are fully coupled; i.e., for $t \gg k_h/u_{\text{West}}^2 \simeq 50$ days), we have $T'_{\text{West}} + T'_{\text{East}} = 0$. Finally, using this equality and simplifying (A4b) yields a set of two boundary conditions for the interior solution in the idealized model:

$$T'_{\text{East}} = -T'_{\text{West}} \quad \text{and} \quad (\text{A6a})$$

$$\partial_x T'|_{\text{East}} = -\partial_x T'|_{\text{West}}. \quad (\text{A6b})$$

APPENDIX B

The Idealized Model Incorporating the Deep Ocean

In this appendix, we describe modifications of (15a) and (15b) necessary to include the effect of the deep ocean.

Firstly, we rename the Fourier amplitudes for temperature at the upper level as T_{cn}^u and T_{sn}^u and introduce two sets of Fourier amplitudes T_{cn}^d and T_{sn}^d for the deep ocean. We neglect the meridional and vertical temperature gradient or mean velocity in the deep ocean because they are very weak relative to those at the surface. We also ignore bottom topography and assume that the deep ocean temperature is controlled only by diffusion. It will be critical, however, that temperature anomalies at depth can change vertical shear in the ocean and modify currents (through thermal wind balance) and hence temperature in the upper ocean. This effect will be included in the equations for T_{cn}^u and T_{sn}^u .

The aforementioned assumptions lead to a new system of equations:

$$\partial_t \begin{pmatrix} T_{cn}^u \\ T_{sn}^u \\ T_{cn}^d \\ T_{sn}^d \end{pmatrix} = \begin{bmatrix} -\kappa \left(\frac{n\pi}{W}\right)^2 & -\frac{n\pi}{W}c & 0 & -\frac{n\pi\tilde{h}}{W}(\hat{u} + c_{\text{Ro}}) \\ \frac{n\pi}{W}c & -\kappa \left(\frac{n\pi}{W}\right)^2 & \frac{n\pi\tilde{h}}{W}(\hat{u} + c_{\text{Ro}}) & 0 \\ 0 & 0 & -\kappa \left(\frac{n\pi}{W}\right)^2 & 0 \\ 0 & 0 & 0 & -\kappa \left(\frac{n\pi}{W}\right)^2 \end{bmatrix} \begin{pmatrix} T_{cn}^u \\ T_{sn}^u \\ T_{cn}^d \\ T_{sn}^d \end{pmatrix}, \quad (\text{B1})$$

where still $c = \bar{u} + \hat{u} + c_{\text{Ro}}$, with $\hat{u} = (\alpha g h \tilde{h} / 2 H f) \partial_y \bar{T}$ and $c_{\text{Ro}} = (-\alpha g \tilde{h}^2 \beta_f / 4 H f^2) \partial_z \bar{T}$.

For a fixed n , a linear stability analysis yields four eigenvalues

$$\lambda_{1,2} = -\kappa \left(\frac{n\pi}{W}\right)^2 \pm i \frac{n\pi}{W}c \quad \text{and} \quad \lambda_{3,4} = -\kappa \left(\frac{n\pi}{W}\right)^2, \quad (\text{B2})$$

corresponding to four eigenvectors

$$\langle \mathbf{u}_{1,2} | = (\mp i, 1, 0, 0), \quad (\text{B3a})$$

$$\langle \mathbf{u}_3 | = c^{-1}[-(\hat{u} + c_{\text{Ro}})\tilde{h}/h, 0, c, 0], \quad \text{and} \\ \langle \mathbf{u}_4 | = c^{-1}[0, -(\hat{u} + c_{\text{Ro}})\tilde{h}/h, 0, c]. \quad (\text{B3b})$$

The corresponding biorthogonal vectors—that is, the eigenvectors of a transposed complex conjugate of the Jacobian matrix defined in (B1)—are

$$\langle \mathbf{u}_{1,2}^\dagger | = (2c)^{-1}[\mp ic, c, \mp i(\hat{u} + c_{\text{Ro}})\tilde{h}/h, (\hat{u} + c_{\text{Ro}})\tilde{h}/h], \quad (\text{B4a})$$

$$\langle \mathbf{u}_3^\dagger | = (0, 0, 1, 0), \quad \text{and} \quad \langle \mathbf{u}_4^\dagger | = (0, 0, 0, 1). \quad (\text{B4b})$$

APPENDIX C

The Idealized Model Incorporating Salinity

In this appendix, we derive a new set of equations for the idealized model, similar to (15a) and (15b), but with

salinity variations included. We first introduce S_{cn} and S_{sn} —the Fourier amplitudes for the upper-ocean salinity

(similar to T_{cn} and T_{sn}). Using a linear equation of state for seawater, we obtain

$$\partial_t \begin{pmatrix} T_{cn} \\ T_{sn} \\ S_{cn} \\ S_{sn} \end{pmatrix} = \begin{bmatrix} -\kappa \left(\frac{n\pi}{W}\right)^2 & A_{1,2} & 0 & A_{1,4} \\ A_{2,1} & -\kappa \left(\frac{n\pi}{W}\right)^2 & A_{2,3} & 0 \\ 0 & A_{3,2} & -\kappa \left(\frac{n\pi}{W}\right)^2 & A_{3,4} \\ A_{4,1} & 0 & A_{4,3} & -\kappa \left(\frac{n\pi}{W}\right)^2 \end{bmatrix} \begin{pmatrix} T_{cn} \\ T_{sn} \\ S_{cn} \\ S_{sn} \end{pmatrix} \quad (C1)$$

with

$$\begin{aligned} A_{1,2} &= -A_{2,1} = -\frac{n\pi}{W} \left(\frac{\alpha g \tilde{h} \tilde{h}}{2Hf} \partial_y \bar{T} - \frac{\alpha g \tilde{h} h^2 \beta_f}{4Hf^2} \partial_z \bar{T} + \bar{u} \right), \\ A_{1,4} &= -A_{2,3} = +\frac{n\pi}{W} \left(\frac{\beta g \tilde{h} \tilde{h}}{2Hf} \partial_y \bar{T} - \frac{\beta g \tilde{h} h^2 \beta_f}{4Hf^2} \partial_z \bar{T} \right), \\ A_{3,2} &= -A_{4,1} = -\frac{n\pi}{W} \left(\frac{\alpha g \tilde{h} \tilde{h}}{2Hf} \partial_y \bar{S} - \frac{\alpha g \tilde{h} h^2 \beta_f}{4Hf^2} \partial_z \bar{S} \right), \text{ and} \\ A_{3,4} &= -A_{4,3} = +\frac{n\pi}{W} \left(\frac{\beta g \tilde{h} \tilde{h}}{2Hf} \partial_y \bar{S} - \frac{\beta g \tilde{h} h^2 \beta_f}{4Hf^2} \partial_z \bar{S} + \bar{u} \right), \end{aligned}$$

where $\partial_y \bar{S}$ and $\partial_z \bar{S}$ are the background meridional and vertical gradients of salinity, and β is the haline contraction coefficient.

The eigenvalues of this system are

$$\lambda_{1,2} = -\kappa \left(\frac{n\pi}{W}\right)^2 \pm i \frac{n\pi}{W} c \quad \text{and} \quad \lambda_{3,4} = -\kappa \left(\frac{n\pi}{W}\right)^2 \pm i \frac{n\pi}{W} \bar{u}, \quad (C2)$$

with the corresponding eigenvectors

$$|\mathbf{u}_{1,2}\rangle = [2(\hat{u} + c_{Ro})]^{-1} \begin{bmatrix} \pm i \left(\frac{g \tilde{h} \tilde{h}}{2Hf} \partial_y \bar{T} - \frac{g \tilde{h} h^2 \beta_f}{4Hf^2} \partial_z \bar{T} \right) \\ \frac{g \tilde{h} \tilde{h}}{2Hf} \partial_y \bar{T} - \frac{g \tilde{h} h^2 \beta_f}{4Hf^2} \partial_z \bar{T} \\ \pm i \left(\frac{g \tilde{h} \tilde{h}}{2Hf} \partial_y \bar{S} - \frac{g \tilde{h} h^2 \beta_f}{4Hf^2} \partial_z \bar{S} \right) \\ \frac{g \tilde{h} \tilde{h}}{2Hf} \partial_y \bar{S} - \frac{g \tilde{h} h^2 \beta_f}{4Hf^2} \partial_z \bar{S} \end{bmatrix} \quad (C3a)$$

and

$$|\mathbf{u}_{3,4}\rangle = (\mp i \beta, \beta, \mp i \alpha, \alpha), \quad (C3b)$$

where $\hat{u} = (g \tilde{h} \tilde{h} / 2Hf)(\alpha \partial_y \bar{T} - \beta \partial_z \bar{S})$ and $c_{Ro} = (g \tilde{h} h^2 \beta_f / 4Hf^2)(-\alpha \partial_z \bar{T} + \beta \partial_z \bar{S})$.

The corresponding biorthogonal vectors [i.e., the eigenvectors of a transposed complex conjugate of the Jacobian matrix defined in (C1)] are

$$\langle \mathbf{u}_{1,2}^\dagger | = (\mp i \alpha, \alpha, \pm i \beta, -\beta) \quad (C4a)$$

and

$$|\mathbf{u}_{3,4}^\dagger\rangle = [2(\hat{u} + c_{Ro})]^{-1} \begin{bmatrix} \mp i \left(\frac{g \tilde{h} \tilde{h}}{2Hf} \partial_y \bar{S} - \frac{g \tilde{h} h^2 \beta_f}{4Hf^2} \partial_z \bar{S} \right) \\ -\frac{g \tilde{h} \tilde{h}}{2Hf} \partial_y \bar{S} + \frac{g \tilde{h} h^2 \beta_f}{4Hf^2} \partial_z \bar{S} \\ \pm i \left(\frac{g \tilde{h} \tilde{h}}{2Hf} \partial_y \bar{T} - \frac{g \tilde{h} h^2 \beta_f}{4Hf^2} \partial_z \bar{T} \right) \\ \frac{g \tilde{h} \tilde{h}}{2Hf} \partial_y \bar{T} - \frac{g \tilde{h} h^2 \beta_f}{4Hf^2} \partial_z \bar{T} \end{bmatrix}. \quad (C4b)$$

REFERENCES

- Arzel, O., T. Huck, and A. Colin de Verdière, 2006: The different nature of the interdecadal variability of the thermohaline circulation under mixed and flux boundary conditions. *J. Phys. Oceanogr.*, **36**, 1703–1718.
- Berloff, P. S., and J. C. McWilliams, 1999: Large-scale low-frequency variability in wind-driven ocean gyres. *J. Phys. Oceanogr.*, **29**, 1925–1949.
- Blanke, B., and P. Delecluse, 1993: Variability of the tropical Atlantic Ocean simulated by a general circulation model with

- two different mixed-layer physics. *J. Phys. Oceanogr.*, **23**, 1363–1388.
- Buckley, M. W., D. Ferreira, J.-M. Campin, J. Marshall, and R. Tulloch, 2012: On the relationship between decadal buoyancy anomalies and variability of the Atlantic Meridional Overturning Circulation. *J. Climate*, **25**, 8009–8030.
- Cessi, P., 2000: Thermal feedback on wind stress as a contributing cause of climate variability. *J. Climate*, **13**, 232–244.
- , and F. Paparella, 2001: Excitation of basin modes by ocean–atmosphere coupling. *Geophys. Res. Lett.*, **28**, 2437–2440.
- Chelton, D. B., and Coauthors, 2007: Global observations of large oceanic eddies. *Geophys. Res. Lett.*, **34**, L15606, doi:10.1029/2007GL030812.
- Chen, F., and M. Ghil, 1995: Interdecadal variability of the thermohaline circulation and high-latitude surface flux. *J. Phys. Oceanogr.*, **25**, 2547–2568.
- Cheng, W., R. Bleck, and C. Rooth, 2004: Multi-decadal thermohaline variability in an ocean–atmosphere general circulation model. *Climate Dyn.*, **22**, 573–590.
- Colin de Verdière, A., 1988: Buoyancy driven planetary flow. *J. Mar. Res.*, **46**, 215–265.
- , and T. Huck, 1999: Baroclinic instability: An oceanic wavemaker for interdecadal variability. *J. Phys. Oceanogr.*, **29**, 893–910.
- Danabasoglu, G., 2008: On multidecadal variability of the Atlantic meridional overturning circulation in the Community Climate System Model version 3. *J. Climate*, **21**, 5524–5544.
- de Boer, A. M., A. Gnanadesikan, N. R. Edwards, and A. J. Watson, 2010: Meridional density gradients do not control the Atlantic overturning circulation. *J. Phys. Oceanogr.*, **40**, 368–380.
- Delworth, T. L., and M. E. Mann, 2000: Observed and simulated multidecadal variability in the Northern Hemisphere. *Climate Dyn.*, **16**, 661–676.
- Dijkstra, H. A., L. A. te Raa, M. J. Schmeits, and J. Gerrits, 2006: On the physics of the Atlantic multidecadal oscillation. *Ocean Dyn.*, **56**, 36–50.
- Dong, B., and R. T. Sutton, 2005: Mechanism of interdecadal thermohaline circulation variability in a coupled ocean–atmosphere GCM. *J. Climate*, **18**, 1117–1135.
- D’Orgeville, M., and W. R. Peltier, 2009: Implications of both statistical equilibrium and global warming simulations with CCSM3. Part II: On the multidecadal variability in the North Atlantic basin. *J. Climate*, **22**, 5298–5318.
- Escudier, R., J. Mignot, and D. Swingedouw, 2013: A 20-yr coupled ocean–sea ice–atmosphere variability mode in the North Atlantic in an AOGCM. *Climate Dyn.*, **40**, 619–636.
- Farrell, B. F., and P. J. Ioannou, 1996: Generalized stability theory. Part I: Autonomous operators. *J. Atmos. Sci.*, **53**, 2025–2040.
- Frankcombe, L. M., and H. A. Dijkstra, 2009: Coherent multidecadal variability in North Atlantic sea level. *Geophys. Res. Lett.*, **36**, L15604, doi:10.1029/2009GL039455.
- , —, and A. von der Heydt, 2008: Sub-surface signatures of the Atlantic multidecadal oscillation. *Geophys. Res. Lett.*, **35**, L19602, doi:10.1029/2008GL034989.
- , —, and —, 2009: Noise-induced multidecadal variability in the North Atlantic: Excitation of normal modes. *J. Phys. Oceanogr.*, **39**, 220–233.
- Gallego, B., and P. Cessi, 2000: Exchange of heat and momentum between the atmosphere and the ocean: A minimal model of decadal oscillations. *Climate Dyn.*, **16**, 479–489.
- Ganachaud, A., and C. Wunsch, 2000: Improved estimates of global ocean circulation, heat transport, and mixing from hydrographic data. *Nature*, **408**, 453–457.
- Gent, P. R., and J. C. McWilliams, 1990: Isopycnal mixing in ocean circulation model. *J. Phys. Oceanogr.*, **20**, 150–155.
- Goldenberg, S. B., C. W. Landsea, A. M. Mestas-Núñez, and W. M. Gray, 2001: The recent increase in Atlantic hurricane activity: Causes and implications. *Nature*, **293**, 474–479.
- Held, I. M., 1983: Stationary and quasi-stationary eddies in the extratropical troposphere: Theory. *Large-Scale Dynamical Processes in the Atmosphere*, B. J. Hoskins and R. P. Pearce, Eds., Academic Press, 127–168.
- Huck, T., and G. K. Vallis, 2001: Linear stability analysis of the three-dimensional thermally-driven ocean circulation: Application to interdecadal oscillations. *Tellus*, **53A**, 526–545.
- , A. Colin de Verdière, and A. J. Weaver, 1999: Interdecadal variability of the thermohaline circulation in box-ocean models forced by fixed surface fluxes. *J. Phys. Oceanogr.*, **29**, 865–892.
- Ioannou, P. J., 1995: Nonnormality increases variance. *J. Atmos. Sci.*, **52**, 1155–1158.
- Johnson, H. L., and D. P. Marshall, 2002: A theory for the surface Atlantic response to thermohaline variability. *J. Phys. Oceanogr.*, **32**, 1121–1132.
- Killworth, P. D., D. B. Chelton, and R. A. de Szoeke, 1997: The speed of observed and theoretical long extratropical planetary waves. *J. Phys. Oceanogr.*, **27**, 1946–1966.
- Knight, J. R., R. J. Allan, C. K. Folland, M. Vellinga, and M. E. Mann, 2005: A signature of persistent natural thermohaline circulation cycles in observed climate. *Geophys. Res. Lett.*, **32**, L20708, doi:10.1029/2005GL024233.
- Kushnir, Y., 1994: Interdecadal variations in North Atlantic sea surface temperature and associated atmospheric conditions. *J. Climate*, **7**, 141–157.
- Latif, M., 1997: Dynamics of interdecadal variability in coupled ocean–atmosphere models. *J. Climate*, **11**, 602–624.
- Levitus, S., 1989: Interpentadal variability of temperature and salinity at intermediate depths of the North Atlantic ocean, 1970–1974 versus 1955–1959. *J. Geophys. Res.*, **94**, 9679–9685.
- Madec, G., and M. Imbard, 1996: A global ocean mesh to overcome the North Pole singularity. *Climate Dyn.*, **12**, 381–388.
- , P. Delecluse, M. Imbard, and C. Lévy, 1998: OPA 8.1 Ocean general circulation model reference manual. IPSL, Note du Pôle de modélisation 11, 91 pp. [Available online at <http://www.nemo-ocean.eu/About-NEMO/Reference-manuals/>]
- Marotzke, J., and J. R. Scott, 1999: Convective mixing and the thermohaline circulation. *J. Phys. Oceanogr.*, **29**, 2962–2970.
- Redi, M. H., 1982: Oceanic isopycnal mixing by coordinate rotation. *J. Phys. Oceanogr.*, **12**, 1154–1158.
- Rosby, C. G., and Coauthors, 1939: Relation between variations in the intensity of the zonal circulation of the atmosphere and the displacements of the semi-permanent centers of action. *J. Mar. Res.*, **2**, 38–55.
- Sévellec, F., and Coauthors, 2009: Non-normal multidecadal response of the thermohaline circulation induced by optimal surface salinity perturbations. *J. Phys. Oceanogr.*, **39**, 852–872.
- Solomon, S., D. Qin, M. Manning, M. Marquis, K. Averyt, M. M. B. Tignor, H. L. Miller Jr., and Z. Chen, Eds., 2007: *Climate Change 2007: The Physical Science Basis*. Cambridge University Press, 996 pp.
- Strogatz, S. H., 1994: *Nonlinear Dynamics and Chaos: With Applications to Physics, Biology, Chemistry, and Engineering*. Perseus, 498 pp.
- Sutton, R. W., and D. L. R. Hodson, 2003: Influence of the ocean on North Atlantic climate variability 1671–1999. *J. Climate*, **16**, 3296–3313.
- , and —, 2005: Atlantic Ocean forcing of North American and European summer climate. *Science*, **309**, 115–118.

- Talley, L. D., J. L. Reid, and P. E. Robbins, 2003: Data-based meridional overturning streamfunctions for the global ocean. *J. Climate*, **16**, 3213–3226.
- te Raa, L. A., and H. A. Dijkstra, 2002: Instability of the thermohaline ocean circulation on interdecadal timescales. *J. Phys. Oceanogr.*, **32**, 138–160.
- , and —, 2003: Sensitivity of North Atlantic multidecadal variability to freshwater flux forcing. *J. Climate*, **16**, 2586–2601.
- , J. Gerrits, and H. A. Dijkstra, 2004: Identification of the mechanism of interdecadal variability in the North Atlantic Ocean. *J. Phys. Oceanogr.*, **34**, 2792–2807.
- Weaver, A. T., J. Vialard, and D. L. T. Anderson, 2003: Three- and four-dimensional variational assimilation with a general circulation model of the tropical Pacific Ocean. Part I: Formulation, internal diagnostics, and consistency checks. *Mon. Wea. Rev.*, **131**, 1360–1378.
- Wunsch, C., and R. Ferrari, 2004: Vertical mixing, energy, and the general circulation of the oceans. *Annu. Rev. Fluid Mech.*, **36**, 281–314.
- Yoshimori, M., C. C. Raible, T. F. Stocker, and M. Renold, 2010: Simulated decadal oscillations of the Atlantic meridional overturning circulation in a cold climate state. *Climate Dyn.*, **34**, 101–121.